DESIGN AND ANALYSIS OF HYBRID WAVEGUIDES FOR LONG RANGE SURFACE PLASMON PROPAGATION

MOHAMMAD SHAFIUL ALAM
(BSc Engg., MIST)
ID NO: 1013160016

A THESIS SUBMITTED FOR THE DEGREE OF MASTERS OF SCIENCE IN ELECTRICAL ELECTRONIC AND COMMUNICATION ENGINEERING

DEPARTMENT OF ELECTRICAL ELECTRONIC AND COMMUNICATION ENGINEERING

MILITARY INSTITUTE OF SCIENCE AND TECHNOLOGY

September 2020

DECLARATION

I hereby declare that the work presented in this thesis is the outcome of the investigation performed by Mr. Mohammad Shafiul Alam under the supervision of Prof. Dr. Md. Shah Alam, Professor, Dept. of EEE, Bangladesh University of Engineering and Technology.

I also declare that no part of this report has been or is submitted elsewhere for the award of any degree in any university previously.

……..

Mohammad Shafiul Alam

ID no. 1013160016

The thesis titled 'DESIGN AND ANALYSIS OF HYBRID WAVEGUIDES FOR LONG RANGE SURFACE PLASMON PROPAGATION' submitted by Mohammad Shafiul Alam, Roll No: 1013160016, Session: 2013-2014 has been accepted as satisfactory in the partial fulfillment of the requirement for the degree of Masters of Science in Electrical Electronic and Communication Engineering on

BOARD OF EXAMINERS

1. _____ Chairman
Prof. Dr. Md. Shah Alam
Professor, Dept. of EEE
Bangladesh University of Engineering and Technology (BUET)

2. _____ Member
Brigadier General A K M Nazrul Islam, PhD (Ex Officio)
Head, Dept. of EECE
Military Institute of Science and Technology (MIST)

3. _____ Member
Air Commodore Md. Hossam-E-Haider, PhD (Retd) (Internal)
Professor, Dept. of EECE
Military Institute of Science and Technology (MIST)

4. _____ Member
Professor Dr. Satya Prasad Majumder (External)
Professor, Dept. of EEE and
Vice-Chancellor
Bangladesh University of Engineering and Technology (BUET)

ABSTRACT

Three different models a metal strip, a slot-based waveguide, and a hybrid plasmonic waveguide with a metal cap have been examined. Comparative analysis of some waveguide characteristics such as propagation length, effective modal area, and Figure of Merit (FOM) was made by varying waveguide dimensions using graphene and regular SiO_2, incorporating the silver as a metal. This research reveals that the lower the waveguide dimension is, the better the outcome for all the models, while conventional SiO_2 is replaced by graphene, which leads this work towards designing nano-scale devices. Firstly, while investigating metal strip waveguides, it was discovered that, regardless of a slight improvement in propagation length and mode area, the figure of merit (FOM) was fundamentally improved (approximately 50%) compared to traditional SiO_2 subsequent to utilizing graphene with a smaller gap among strip and the metal substrate. Furthermore, the highest propagation length was 8.5 μm, which is about 75% higher than that of SiO_2. Then secondly, the slot-based waveguide was examined. The largest propagation length was found as 224 μm using SiO_2 when the height of silver was 50 nm, silicon layer between metal (d_s) was 70 nm with a metal width of 40 nm, though the highest figure of merit was limited to 4951 by setting d_s at 60nm. The results were better using SiO_2 rather than graphene, which was quite the opposite of the direction of this research. Thus, the third model, a hybrid plasmonic waveguide with a graphene layer and metal cap on top, was introduced, which demonstrates an elevated propagation length 1814 μm with tight confinement of around 250 nm^2. The key parameter, the figure of merit, is found in the range of 10^6 when we keep graphene layer 5 nm, utilized in the middle of metal and silicon, which is not only superior to that of the SiO_2 layer but also the highest values of FOM found in previous models. In this manner, among three models, a hybrid plasmonic waveguide with a metal cap shows a better outcome regarding propagation length, modal area, and Figure of merit.

ACKNOWLEDGEMENTS

Firstly, I offer my heartiest gratefulness to the most graceful and most merciful Allah for his kindness and infinite magnanimity bestowed on me that I can complete this thesis paper. I am also grateful to the Department of Electrical and Electronic Communication Engineering of Military Institute of Science and Technology for providing support during this research work.

I feel the honor to offer our immeasurable heartiest gratitude and profound indebtedness to professor Dr. Md. Shah Alam, for his constant support and guidance during this research work, starting from the development of the thesis proposal until the writing of this thesis. His careful reading of the draft, valuable comments, criticism, and constructive suggestions immensely contributed to the improvement of this thesis work.

I wish to express heartfelt thanks to my parents, sister, and friends for their constant encouragement.

TABLE OF CONTENTS

LIST OF FIGURES

LIST OF SYMBOLS

β	propagation constant
k	wave number
λ	wavelength
μ	permeability
ε	permittivity
ω_p	Plasmon frequency
ρ	charge density
τ	damping time
γ	damping rate
J	current density
σ	static conductivity

LIST OF ABBREVIATIONS

SPP	Surface Plasmon Polariton
TEM	Transverse Electro-Magnetic
FOM	Figure of Merit
EM	Electro-Magnetic
TE	Transverse Electric
LRSPP	long Range Surface Plasmon Polariton
IMI	Insulator-metal- insulator
MIM	Metal- insulator – metal
HSPP	Hybrid Surface Plasmon Polariton
PML	Perfectly matched layer
PDE	Partial Differential Equation
FEM	Finite element method

Chapter 1

INTRODUCTION

1.1 Introduction

With the advancement of modern science, the flow of light has been manipulated in various ways for using in wide variety of applications in the field of science and technology. Several natural phenomena, from the skill of scale of cell division to birth of giant stars, could be visualized through different interactions between light, dielectric lenses, and metallic mirrors. At present, the utilization of light is not just confined within imaging. Instead, it has created enormous possibilities.

1.2 Plasmonics and Hybrid Waveguides

Light confinement is such a field of research these days enabling light to be used in macroscale application. The use of light in telecommunication offers extremely higher bandwidth and lower wastage of power with significantly improved latency compared to wired or electronic connection [18]. Using the similar concept, photonic could be used in a smaller scale such as interconnecting chips or nanodevices, which will ensure low power dissipation and higher ability of computation. Lowering the scale of optical components to nanoscale electronic components would depend on how efficiently the photonics would be integrated with electronics [19]. The absorption of the maximum portion of incident light by a solar panel may be ensured by introducing an efficient technique of absorption of solar light by the material, and hence, the conversion rate of photovoltaic energy could be increased. This, eventually, will lower the cost of materials, raise the efficiency and even, will create more availability of materials, including conventional and unconventional. Also, enhanced efficiency refers to concentrating more light, which will increase the accuracy in the field of

various types of sensor applications[20-22]. Additionally, interactions that are non-linear will be more precise and robust [23].

Higher confinement of light will result in increased photonic mode concentration thus if an emitter placed in such a strong and highly dense optical field will radiate more than it will do in the free space [24]. This is crucial in the field of applications of light-emitting diode (LED), lasers, and quantum information field where emitters have to be appropriately integrated with the photonic circuits [25].

The wavelength of light has made the existing techniques of concentrating light to the smallest scale, such as using lenses or mirrors, limited. The reason behind this limitation is the diffraction around the edge of the aperture of those optical devices. In this case, there is a minimum distance between constructive and destructive interference after diffraction despite having a large aperture. The Fourier transform shows that the order of the size of the one-dimensional plane Δx to which a plane light can be focused can be shown as [16]

$$\Delta x \approx \frac{2\pi}{\Delta k_x} = \frac{\lambda_0}{2} \tag{1.1}$$

Here, the maximum possible spread of the wavevector component k_x along the x-direction is expressed as $\Delta k = 4\pi/\lambda_0$, whereas λ_0 denotes the wavelength in vacuum. Alternatively, the separation between two objects is administered by the length of this scale, and the objects are clearly identifiable from each other under a microscope.

Light-matter interactions on a metal surface can be a decent way to of light confinement beyond the capacity of typical lenses or dielectric structures. Surface plasmon polariton can be referred to as evanescent electromagnetic waves, which is bolstered by the metal-dielectric interface. The coherent oscillation of the free charges, at the metal surface, assists in strongly couples with the interface. This is how the optical energy can propagate through some small

dimensions. Recently, the field of plasmonics is extensively researched due to the ability of strong light confinement and applicability in the advancing field of nanotechnology [19-27].

Realization of subwavelength based optical chips/devices are one step closer due to tightly confined plasmon polaritons modes supported by designed structures like waveguides. In addition, this waveguiding scheme based on metal and plasmonic concept can be potential scope for carrying both electronic and optical signals through the same metal structure. This means the combined plasmonic and electronic nature of the device would ensure enhanced data capacity and flawless optical signal transmission at the nanoscale. Although propagation loss is unavoidable in plasmonic waveguide because of interaction between mode and the metal, this propagation loss is traded off with localization of the optical mode. For example, the SPP distance can be reduced by using the strong interaction between the electromagnetic field and the metal. This is also supported by the smaller size of the mode and tighter confinement. Hybrid waveguides are being a good candidate to address the existing challenge and being studied by researchers.

It is common that hybrid waveguides are made up of a metal surface and a spacer of low refractive index with a medium of high refractive index in between. In this type of structure, both plasmonic and photonic features assist in guiding the electromagnetic energy, which is confined between the materials of high and low refractive index. This dual characteristic (plasmonic and photonic) offers diversified modal characteristics in terms of strong confinement and larger value of propagation length, which can simply be adjusted by changing the dimension of the gap and refractive index of the material.

1.3 Literature Review

The plasmonic waveguides have enormous applications in the modern era of waveguiding.

Surface plasmon polaritons (SPPs) are electromagnetic waves that propagate along the edge of the metal and dielectric interface. There are two kinds of surface plasmons depicted as surface plasmon polaritons and localized surface plasmons. The explanation for picking and examining the surface plasmon polaritons for nanophotonic circuits is its extraordinary engendering attributes and a high degree of confinement, which can be expressed by classical physics [1]-[2]. Though there is diffraction, SPP gives long-range propagation along the metal surface, which enables the fabrication of equipment at the terahertz regime in the sub-wavelength level [3]. There are lots of recommendations and experimental trial of SPP waveguides, for example, Spoof SPP structure, thin metal films, chemically synthesized metal nanowires (NWs), and sharp metal wedge structures to guide SPPs for potential nanophotonic devices, e.g, nano-lasers, couplers, switches, modulators, and biosensors [4]-[8]. A high degree of confinement in the plasmonic waveguide costs high loss due to the use of metal. So, despite having very low propagation loss, the optical performance is also very low because of the large mode area due to the weak modal confinement in the plasmonic waveguides with a single dielectric.

The main challenges while designing plasmonic waveguides are high-frequency operation and nanometer range fabrication. Thus, to provide better propagation along with sub-wavelength confinement, hybrid waveguides are proposed [9]. These types place a lower index insulator layer in the nanometer level between the metal and dielectric material, which is the reason behind the reduced ohmic loss [10]. While designing plasmonic waveguide with enhanced transmission property, a series of investigations have been performed with different hybrid models to achieve a higher level of confinement with elevated propagation characteristics [11]-[13]. Initially, a dielectric-metal-dielectric sandwich structure is used with a small layer of lower index semiconductor material, to reduce the energy loss in plasmon modes. While designing plasmonic integrated circuits, these types of waveguides

use the coupling between the SPP and the conventional dielectric mode for nano-scale applications [11]. Later in another study, it was found that two nanorods of dielectrics separated by a metal slab having a small layer of low indexed dielectric in between, provides lower diffraction and tight confinement as well as higher propagation length. This design was not promising enough because of the complicated design process and weak confinement. However, the structures are used as nanolasers and optical signal processing devices [12]. Then a simpler rectangular hybrid model is proposed with a dielectric (Si) rib and a metal cap (Ag) on SiO_2 substrate, which is relatively easy to fabricate. In between Ag and Si there is a lower indexed dielectric layer of SiO_2 [13]. The ohomic loss is lower due to the discontinued layers of two dissimilar dielectric materials- silica and silicon with different refractive indexes, which provide enhanced confinement. The field of the guided hybrid mode is confined more in the low index dielectric gap region [14].

Here in this work, at first, a strip and slot based waveguides have been considered to compare performance between SiO_2 and graphene followed by a hybrid waveguide with metal cap and graphene. In every case, the propagation length, effective modal area, and finally, Figure of Merit (FOM) have been used as the factors for comparison. In the case of metal strip waveguide, better results were found after using graphene instead of SiO_2. The results for slot based hybrid waveguide was just the opposite after using graphene rather than SiO_2. In the case of the hybrid waveguide with metal cap and graphene, graphene is used in replace of SiO_2 layer in between Ag and Si. As a semi-metal, graphene can direct the electron in plasma wavelength, results in a reduction of ohomic loss introduced by the metal. Graphene also leads to lower optical losses and tight confinement due to some change in the Fermi level, which enhance the tunability of absorption for electromagnetic energy [15]-[16]. It is highly suitable for fabrication in the nanometer range, and the dispersion effect is very negligible caused by scattering and other losses in this region if the waveguide length is minimal [17].

1.4 Objectives of the Work

The objectives of the proposed research are:

a. To study Surface Plasmon polariton concept
b. To develop new device models using SPP applications.
c. To implement the new technique and evaluate its performance for the specific models of SPP waveguides.
d. To determine the highest Figure of merit of the specific models of SPP waveguide and compare the relative performance among them.

The possible outcomes of the research will be understanding the approach towards the development of photonic devices and achieve better parameters in the applications of these devices. Successful completion of the proposed research would significantly contribute to the development of a photonic application such as SPP Nano laser, photonic switch, and optical modulators.

1.5 Organization of the Thesis

The whole design has been done by using COMSOL Multiphysics^{TM} simulation software, where experimental data clearly represents the superiority of the design. The whole work has been organized as,

1) analysis of previous design of strip, metal strip, and hybrid plasmonic waveguides with a metal cap with SiO_2,

2) repetition of step 1, with Graphene in place of SiO_2,

3) visualization and comparison between the power distribution/confinement for all three types of waveguides and

4) repetition of all the previous steps while using graphene.

This thesis paper is organized as follows,

- **Chapter 1** discusses some introductory topics, including plasmonics, waveguides, literature review, and a brief overview and structures of the work
- **Chapter 2** discusses some theoretical backgrounds on surface plasmon polaritons. It also discusses applications of Maxwell's and Helmholtz equations, electromagnetic waveguides and their modes, plasmonic and hybrid waveguides, and materials.
- **Chapter 3** discusses the analysis techniques such as COMSOL and finite element analysis, PDEs and boundary conditions, meshing, different SPP modes, and methodologies of the works at the end.
- **Chapter 4** shows the results and discusses them based on the approaches and designs that have been considered in work.
- **Chapter 5** concludes the works with a summary and future recommendations

Chapter 2

THEORETICAL BACKGROUND

2.1 Introduction

In this chapter, the necessary theoretical background has been discussed to provide fundamental knowledge on the characteristic of surface plasmon polaritons. At the very beginning, Maxwell's equation has been discussed in various forms, which are considered as the basic equation in the field of electromagnetism followed by boundary conditions. In this chapter, how metal behaves in the electromagnetic domain is discussed with the help of the Drude model. Waveguides are referred to as the device to guide electromagnetic waves in a confined and guided manner. A number of modes are used while guiding the wave, and this chapter explains different aspects of modes. Additionally, while considering waveguides, the selection of material is an issue, and this part of the thesis work includes a brief discussion on that. Finally, SPPs waveguiding has been discussed in detail. This includes important characteristics and features of a dielectric-loaded waveguide and hybrid waveguides.

2.2 Maxwell's Equations

Electromagnetic phenomena that are macroscopic can be explained through Maxwell's four partial equations [15]. The equations can be written both in differential form and integral form. Maxwell's equations are stated below:

Table 2.1 Maxwell's electromagnetic wave equation

Integral Form	Differential Form
$\iint_S \vec{D} \cdot \hat{n}\, dS = q$	$\nabla \cdot \vec{D} = \rho_{ext}$

Integral Form	Differential Form
$\iint_S \vec{B} \cdot \hat{n}\, dS = 0$	$\nabla \cdot \vec{B} = 0$
$\oint_C \vec{E} \cdot \hat{t} dC = -\frac{\partial}{\partial t} \iint_S \vec{B} \cdot \hat{n}\, dS$	$\nabla \times \vec{E} = -\frac{\partial \vec{B}}{\partial t}$
$\oint_C \vec{H} \cdot \hat{t} dC = I + \frac{\partial}{\partial t} \iint_S \vec{H} \cdot \hat{n}\, dS$	$\nabla \times \vec{H} = \vec{J}_{ext} + \frac{\partial \vec{D}}{\partial t}$

The four macroscopic fields are further linked via the polarization $\vec{P}$ and magnetization $\vec{M}$ by

$$\vec{D} = \varepsilon_0 \vec{E} + \vec{P} \tag{2.1}$$

$$\vec{H} = \frac{\vec{B}}{\mu_0} - \vec{M} \tag{2.2}$$

where ε_0 and μ_0 are the electric permittivity and magnetic permeability of vacuum, respectively. Here magnetic response, $\vec{M}$, can be ignored since only nonmagnetic media has been considered. But $\vec{P}$ represents the dipole moment withing the material which is created by It describes the electric dipole moment per unit volume inside the material, caused by the placement of the dipoles at the microscopic level according to the applied electric field. The relation between this and internal charge density ρ can be written as

$$\nabla . \vec{P} = -\rho \tag{2.3}$$

Charge conservation

can be expressed as $\nabla . \vec{J} = -\frac{\partial \rho}{\partial t}$, which requires the following relationship between internal charge and current densities.

$$\vec{J} = \frac{\partial \vec{P}}{\partial t} \tag{2.4}$$

Now as $\nabla . \vec{D} = \varepsilon_0 \nabla . \vec{E} + \nabla . \vec{P} = \rho_{ext}$ and $\nabla . \vec{P} = -\rho$, (2.5a,b)

$$\nabla . \vec{E} = \frac{\rho_{ext} + \rho}{\varepsilon_0} = \frac{\rho_{tot}}{\varepsilon_0} \tag{2.5c}$$

For linear, isotropic and nonmagnetic media

$$\vec{D} = \varepsilon_0 \varepsilon \vec{E} \tag{2.6}$$

$$\vec{B} = \mu_0 \mu \vec{H} \tag{2.7}$$

where ε is called the dielectric constant or relative permittivity and $\mu = 1$ is the relative permeability of the nonmagnetic medium.

2.3 Boundary Conditions

At an interface between two media, as shown in fig 2.1, the certain boundary condition is to be satisfied.

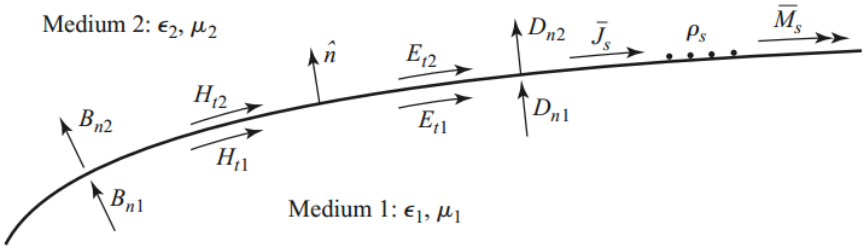

Fig. 2.1 : Fields and surface charge at an interface between two media [1]

The boundary conditions are:

$$\hat{n}.(\overrightarrow{D_2} - \overrightarrow{D_1}) = \rho_s, \text{ or } D_{2n} - D_{1n} = \rho_s \tag{2.8a}$$

$$\hat{n}.\overrightarrow{B_2} = \hat{n}.\overrightarrow{B_1} \tag{2.8b}$$

$$(\overrightarrow{E_2} - \overrightarrow{E_1}) \times \hat{n} = \overrightarrow{M_s} \tag{2.8c}$$

$$\hat{n} \times (\overrightarrow{H_2} - \overrightarrow{H_1}) = \overrightarrow{J_s} \tag{2.8d}$$

Here ρ_s is the surface charge density, $\overrightarrow{M_s}$ is the magnetic surface current density and $\overrightarrow{J_s}$ is an electric surface current density on the interface.

When no charge or surface current densities exist, the above equations reduce to

$$\hat{n}.\overrightarrow{D_2} = \hat{n}.\overrightarrow{D_1} \tag{2.9a}$$

$$\hat{n}.\overrightarrow{B_2} = \hat{n}.\overrightarrow{B_1} \tag{2.9b}$$

$$\hat{n} \times \overrightarrow{E_2} = \hat{n} \times \overrightarrow{E_1} \tag{2.9c}$$

$$\hat{n} \times \overrightarrow{H_2} = \hat{n} \times \overrightarrow{H_1} \tag{2.9d}$$

The above equations indicate the continuity of normal components of $\vec{D}$ and $\vec{B}$ and tangential components of $\vec{E}$and $\vec{H}$ across the boundary.

2.4 The Helmholtz Wave Equation

In the absence of external charge and current densities, the curl equations can be combined to yield [28]:

$$\nabla \times \nabla \times \vec{E} = -\mu_0 \frac{\partial^2 \vec{D}}{\partial t^2} \tag{2.10}$$

We are assuming that those external stimuli $\nabla.\vec{D} = 0$ is absent, and involving the identities $\nabla \times \nabla \times \vec{E} = \nabla(\nabla.\vec{E}) - \nabla^2\vec{E}$ and $\nabla(\varepsilon\vec{E}) \equiv \vec{E}.\nabla\varepsilon + \varepsilon\nabla.\vec{E}$ (2.10) can be rewritten as

$$\nabla(-\frac{1}{\varepsilon}\vec{E}.\nabla\varepsilon) - \nabla^2\vec{E} = -\mu_0\varepsilon_0\varepsilon\frac{\partial^2\vec{E}}{\partial t^2} \tag{2.11}$$

For a negligible variation of the dielectric profile over distances on the order of one optical wavelength, (2.9) simplifies to the central equation of electromagnetic wave theory,

$$\nabla^2\vec{E} - \frac{\varepsilon}{c^2}\frac{\partial^2\vec{E}}{\partial t^2} = 0 \tag{2.12}$$

The equation is to be solved separately in regions of constant ε , and the obtained solutions have to be matched using appropriate boundary conditions.

For harmonic time dependence,

$$\vec{E}(\vec{r},\mathrm{t}) = \vec{E}(\vec{r})\,\mathrm{e}^{i\omega t} \tag{2.13a}$$

Inserted into (2.10), this yields

$$\nabla^2\vec{E} + k_0^2\varepsilon\vec{E} = 0 \tag{2.13b}$$

where, $k_0 = \dfrac{\omega}{c}$ and $k_0^2\varepsilon = k_x^2 + k_y^2 + k_z^2$

$k_0 = \dfrac{\omega}{c}$ is the wave vector of the propagating wave in vacuum for $\vec{E}$. k_x, k_y, k_z are the respective wave vector along x, y, and z-axis. Equation (2.11) is known as the **Helmholtz** equation. An identical equation for $\vec{H}$ be derived in the same manner:

$$\nabla^2\vec{H} + k_0^2\varepsilon\vec{H} = 0 \tag{2.13c}$$

2.5 Electromagnetic Behavior of Metal According to the Drude Model

In the classical Drude model, metal is assumed to contain a large number of free electrons. Once a background of positive ion core is set against these electrons, they resemble the gas of electrons. The movement of these electrons, however, is decelerated by a peripheral electric field, causing the cores hit by electrons. The Drude model neglects all interactions during collisions. The behavior of these electrons can be modeled with Lorentz harmonic oscillator model.

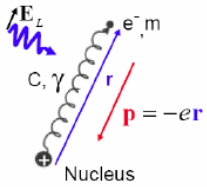

Fig. 2.2 Interaction of electromagnetic waves with electron bound to the nucleus[1].

An individual electron's motion is governed by the following equation of motion

$$m\vec{a}_e = \vec{F}_{E,local} + \vec{F}_{damping} + \vec{F}_{spring}$$

for applied electric field $\vec{E}_L$:

$$-e\vec{E}_L = m\frac{\partial^2\vec{r}}{\partial t^2} + m\gamma\frac{\delta\vec{r}}{\delta t} + C\vec{r} \tag{2.14}$$

where, m is the mass of an electron, C is related to hypothetical spring between an electron and positively charged ion and γ is related to the damping of the oscillation

According to the Drude model, an electron is not bound to any particular nucleus, so C=0 and the above equation becomes

$$-e\vec{E}_L = m\frac{\partial^2\vec{r}}{\partial t^2} + m\gamma\frac{\delta\vec{r}}{\delta t} \tag{2.15a}$$

Using $\vec{v} = \frac{\delta\vec{r}}{\delta t}$, $$-e\vec{E}_L = m\frac{\delta\vec{v}}{\delta t} + m\gamma\vec{v}$$

$$-e\vec{E}_L = m\frac{\delta\vec{v}}{\delta t} + \frac{m}{\tau}\vec{v} \tag{2.15b}$$

here $\tau = \frac{1}{\gamma}$ is the relaxation time ($\approx 10^{-14} s$)

The current density is defined as $$\vec{J} = -Ne\vec{v}$$

Substituting in the equation (2.15a)

$$-e\vec{E}_L = -\frac{m}{Ne}\frac{\delta\vec{J}}{\delta t} - \frac{m}{\tau Ne}\vec{J}$$

Rearranging we get $$\frac{\delta\vec{J}}{\delta t} + \frac{1}{\tau}\vec{J} = \frac{Ne^2}{m}\overrightarrow{E_L} \quad (2.15c)$$

Assuming sinusoidal variation of an electric field $\overrightarrow{E_L} = \overrightarrow{E_0}\,exp(-i\,\omega\,t)$ and current density $\vec{J} = \overrightarrow{J_0}\,exp(-i\,\omega\,t)$the equation becomes

$$\frac{\delta(\overrightarrow{J_0}\,exp(-i\,\omega\,t))}{\delta t} + \frac{1}{\tau}\overrightarrow{J_0}\,exp(-i\,\omega\,t) = \frac{Ne^2}{m}\overrightarrow{E_0}\,exp(-i\,\omega\,t)$$

$$(-i\omega + \tfrac{1}{\tau})\overrightarrow{J_0} = (\tfrac{Ne^2}{m})\vec{E}_0$$

$$(-i\omega + \tfrac{1}{\tau})\vec{J} = (\tfrac{Ne^2}{m})\vec{E}$$

For static field, ω=0 and

$$\vec{J} = (\tfrac{Ne^2\tau}{m})\vec{E} = \sigma\vec{E}$$

where $\sigma = \dfrac{Ne^2\tau}{m}$ is called static conductivity

For the general case of the oscillating field

$$\vec{J} = (\tfrac{\sigma}{1-i\omega\tau})\vec{E} = \sigma_\omega\vec{E} \quad (2.16)$$

where $\sigma_\omega = (\dfrac{\sigma}{1-i\omega\tau})$ is known as dynamic conductivity. This is purely a real number if the frequency is kept very low ($\omega\tau << 1$). In this case, the electric field is fully followed by the electrons. However, the movement of the electron starts to lag, and dynamic conductivity becomes complex once the frequency starts to increase. For a very high frequency, $\omega\tau >> 1$

the dynamic conductivity of electron is purely imaginary, and the electron oscillation is 90 degrees out of phase with the applied electric field.

For metal, Maxwell wave equation (2.13b) gives assuming $\vec{P} = 0$ and $\vec{J} \neq 0$

$$\nabla^2\vec{E} + (\omega^2\mu\varepsilon_0 + i\omega\mu\sigma_\omega)\vec{E} = 0 \qquad (2.17)$$

This equation is satisfied by the electric fields of the forms $\vec{E} = \overrightarrow{E_p}\, exp(-i(\vec{k}.\vec{r}))$ with an implicit $\exp(-\mathrm{i}\omega\mathrm{t})$ variation where

$$k^2 = \omega^2\mu\varepsilon_0 + i\omega\mu\sigma_\omega \quad . \qquad (2.18)$$

As metal permeability is very close to the permeability of free space. So,

$$c^2 = \frac{1}{\mu_0\varepsilon_0} \qquad (2.19)$$

where c is the velocity of the light wave in the vacuum.

Then we get from Equation 2.18

$$k^2 = \frac{\omega^2}{c^2} + i\omega\mu_0\sigma_\omega \qquad (2.20)$$

Again the refractive index of a medium is $n^2 = \frac{c^2}{\omega^2}k^2$

So, $$n^2 = \frac{c^2}{\omega^2}\left(\frac{\omega^2}{c^2} + i\omega\mu_0\sigma_\omega\right)$$

$$n^2 = 1 + \frac{ic^2\mu_0\sigma_\omega}{\omega}$$

$$n^2 = 1 + \frac{ic^2\mu_0\sigma}{\omega(1-i\omega\tau)} = 1 + i\frac{i\tau}{i\tau}\frac{c^2\mu_0\sigma}{\omega(1-i\omega\tau)} = 1 - \frac{\frac{c^2\mu_0\sigma}{\tau}}{\omega\left(\frac{i}{\tau}+\omega\right)} = 1 - \frac{\frac{c^2\mu_0\sigma}{\tau}}{\omega^2 + \mathrm{i}\frac{\omega}{\tau}} \qquad (2.21)$$

The plasma frequency is defined as $$\omega_p = \frac{c^2\mu_0\sigma}{\tau} \qquad (2.22)$$

putting value of σ

$$\omega_p{}^2 = \frac{c^2\mu_0}{\tau}\frac{Ne^2\tau}{m} = \frac{Ne^2c^2\mu_0}{m} = \frac{Ne^2}{m\varepsilon_0} \tag{2.23}$$

The refractive index of the medium can be expressed as

$$n^2 = 1 - \frac{\omega_p{}^2}{\omega^2 + \mathrm{i}\frac{\omega}{\tau}} \tag{2.24}$$

Now dielectric constant of a material

$$\varepsilon(\omega) = n^2 = 1 - \frac{\omega_p{}^2}{\omega^2 + i\frac{\omega}{\tau}} = 1 - \frac{\omega_p{}^2\left(\omega^2 - i\frac{\omega}{\tau}\right)}{\left(\omega^2 + i\frac{\omega}{\tau}\right)\left(\omega^2 - i\frac{\omega}{\tau}\right)}$$

$$\varepsilon(\omega) = 1 - \frac{\omega_p{}^2(\omega^2 - i\frac{\omega}{\tau})}{\omega^4 + \frac{\omega^2}{\tau^2}} = (1 - \frac{\omega_p{}^2}{\omega^2 + \frac{1}{\tau^2}}) + i(\frac{\frac{\omega_p{}^2}{\tau}}{\omega^3 + \frac{\omega}{\tau^2}}) \tag{2.24b}$$

So, the real part of dielectric constant $\varepsilon_r = 1 - \dfrac{\omega_p{}^2}{\omega^2 + \dfrac{1}{\tau^2}}$

(2.24a)

and imaginary part of dielectric constant $\varepsilon_i = \dfrac{\dfrac{\omega_p{}^2}{\tau}}{\omega^3 + \dfrac{\omega}{\tau^2}}$ (2.24c)

This equation was derived, assuming no inter-band transition. Typically ω_p is on the order of 10^{15} and $\frac{1}{\tau}$ is on the order of 10^{12}. Metal behavior for different frequency regimes can be predicted based on this equation.

High-frequency regime ($\omega >> \frac{1}{\tau}$):

$$\varepsilon_r = 1 - \frac{\omega_p^{\ 2}}{\omega^2} \qquad \text{and} \qquad \varepsilon_i = \frac{\omega_p^{\ 2}}{\omega^3 \tau} \tag{2.24d}$$

So dielectric function is mostly real with negligible imaginary part and damping. In this region, metal acts as a dielectric material rather than a metal. For $\omega < \omega_p$ real part of dielectric function is negative and for $\omega > \omega_p$ real part of dielectric function is positive

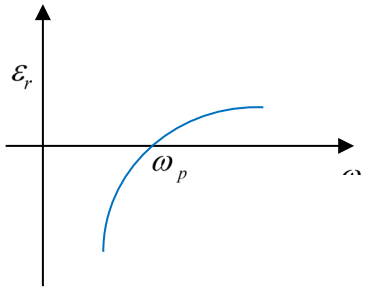

Fig 2.3 The variation of real part of dielectric constant in high-frequency regime.

In reality, metal behavior in this regime is completely altered by inter-band transition leading to an increase in ε_i

Low-frequency regime ($\omega << \frac{1}{\tau}$): $\varepsilon_r = 1 - \omega_p^{\ 2}\tau^2$ and $\varepsilon_i = \frac{\omega_p^{\ 2}\tau}{\omega}$

So, the real part of the dielectric constant is negative, and the imaginary part of the dielectric constant has a very high positive value. In the case of metals, those are nobles such as Au, Ag, Cu, a highly polarized environment is created due to the close proximity of the filled d band to the Fermi surface. Hence, in the region of $\omega > \omega_p$, the above model is needed to be extended for those metals.

$$\varepsilon(\omega) = \varepsilon_\infty - \frac{\omega_p^{\ 2}}{\omega^2 + \mathrm{i}\frac{\omega}{\tau}} \tag{2.25}$$

In general, although ε_∞ can change according to wavelength and normally is termed as Lorentz oscillator [16], this value is assumed as constant for some ranges within the spectrum. Additionally, a plasmonic particle can alter the value of $\gamma = \frac{1}{\tau}$. The classical theory states that the overall rate of damping γ is made up of scatterings between electrons and phonons, and grain-boundary or lattice defects scattering. Plasmonic particle's size affects the rate of boundary scattering, and assuming the size of a spherical particle as R, the rate of relaxation can be expressed as:

$$\gamma = \gamma_\infty + A\frac{v_F}{R} \tag{2.26}$$

where R is the relaxation constant of the bulk material v_F is the Fermi velocity; the process of scattering has an impact on the value of A, and is typically on the order of unity [17]. For simplicity, below, we assume that $\gamma = \gamma_\infty$. Table 2.2 shows the Drude model parameter of common metals. Here ω_∞ is the frequency of onset for interband transitions. Drude parameters tabulated are not valid beyond this frequency. The validity of the Drude model for silver (it is used as metal in this thesis) is shown in Fig. 2.4.

Table 2.2 Drude model parameter of common metals

	ε_∞	$\omega_p (10^{15}$ Hz)	$\gamma = \frac{1}{\tau} (10^{12}$ Hz)	$\omega_\infty (10^{14}$ Hz)
Silver [18]	3.7	2.2	4.83	9.42
Gold [18]	6.9	2.15	1.69	5.55
Copper [18]	6.7	2.1	1.69	5.07

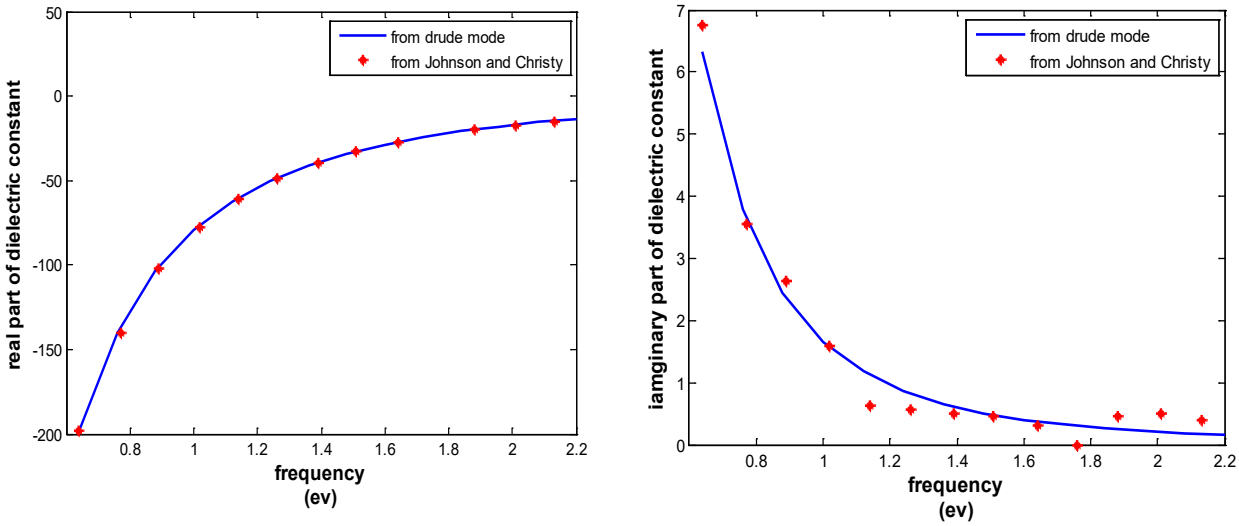

(a) real part (b) imaginary part

Fig. 2.4 The real and imaginary part of $\varepsilon(\omega)$ for silver determined by Johnson and Christy[34] (red asterisk) and Drude model (solid blue line).

2.6 Electromagnetic Wave Propagation

Understanding the propagation of SPP mode required extensive knowledge in the propagation of electromagnetic (EM) waves. All EM phenomena are governed by Maxwell's equations [1]. The symmetry and duality of Maxwell's equations are evident in a source-free region. These equations can be validated in the regions that contain charges and currents; however, the existence of electric charges and without the magnetic ones make Maxwell's equations asymmetric[30]. This symmetry can be restored if magnetic monopoles are allowed mathematically. The source-free Maxwell's equations for the case that $J_m = J_e = 0$ and $\rho_m = \rho_e = 0$ and are valid when there are no freely moving charges. From these Maxwell's equations stated in table 2.1, we can derive wave equations of the form [28]:

$$\nabla^2 E - \mu\epsilon \frac{\partial^2 E}{\partial t^2} = -(\nabla\tilde{\epsilon}.\nabla)E - (E.\nabla)\nabla\tilde{\epsilon} - \nabla(\tilde{\epsilon} + \tilde{\mu}) \times (\nabla \times E) \qquad (2.27a)$$

$$\nabla^2 B - \mu\epsilon \frac{\partial^2 B}{\partial t^2} = -(\nabla\tilde{\mu}.\nabla)B - (B.\nabla)\nabla\tilde{\mu} - \nabla(\tilde{\mu} + \tilde{\epsilon}) \times (\nabla \times B) \qquad (2.27b)$$

for spatially dependent permittivity and permeability here,

$$\tilde{\epsilon} = \ln \epsilon \ , \quad \tilde{\mu} = \ln \mu \tag{2.28}$$

and *E* and *B* are the incident electric and magnetic fields.

For spatially invariant permittivity and permeability eq. 2.27 reduce to:

$$\nabla^2 E - \mu\epsilon \frac{\partial^2 E}{\partial t^2} = 0 \tag{2.28}$$

$$\nabla^2 B - \mu\epsilon \frac{\partial^2 B}{\partial t^2} = 0 \tag{2.29}$$

These equations are second-order partial differential equations and can be solved for the EM fields. Again, considering time-harmonic dependence for the electromagnetic (EM field), then, $\frac{\partial}{\partial t} = -i\omega$

where i is the imaginary unit, and ω is the angular frequency. In this case, Maxwell's equations can be express in cartesian co-ordinates as follows [1]:

$$\frac{\partial E_z}{\partial y} - \frac{\partial E_y}{\partial z} = i\omega\mu_0 H_x \tag{2.30}$$

$$\frac{\partial E_x}{\partial z} - \frac{\partial E_z}{\partial x} = i\omega\mu_0 H_y \tag{2.31}$$

$$\frac{\partial E_y}{\partial x} - \frac{\partial E_x}{\partial y} = i\omega\mu_0 H_z \tag{2.32}$$

$$\frac{\partial H_z}{\partial y} - \frac{\partial H_y}{\partial z} = -i\omega\varepsilon_0 \varepsilon E_x \tag{2.33}$$

$$\frac{\partial H_x}{\partial z} - \frac{\partial H_z}{\partial x} = -i\omega\varepsilon_0 \varepsilon E_y \tag{2.34}$$

$$\frac{\partial H_y}{\partial x} - \frac{\partial H_x}{\partial y} = -i\omega\varepsilon_0 \varepsilon E_z \tag{2.35}$$

2.7 Electromagnetic Waveguides

The propagation, control, and confinement of electromagnetic energy are accomplished by waveguides [27]. Waveguides are based on different electric and magnetic materials with

negative and positive EM susceptibilities. The applications of these structures, such as in radars and optical fibers, provide motivation for further advances in this field. Waveguides can be made of different structures, such as rectangular, slab, and cylindrical geometries. Among different structures of waveguides, rectangular, slab, and cylindrical are widely used and based on the type's materials and geometry. Waveguides can be characterized [27].

Waveguide modes

The waveguide modes refer to the cross-section of energy distribution in the waveguide core. In fact, modes are eigenvectors of eigenvalue equations. Solutions of Maxwell's equations, along with satisfying the boundary conditions, yield a transcendental dispersion equation. For a given frequency, the transcendental dispersion equation may yield a finite number of roots for the propagation coefficient. These discrete roots represent the eigenvalues of the modes. Eigenvectors corresponding to these eigenvalues that respect the boundary conditions are modes. For a given frequency, there may be a case where no real root of the propagation coefficient exists. In that case, a guided mode simply does not exist for that situation. The mode's behavior in a waveguide depends on parameters including waveguide materials, geometry, and the frequency of the EM wave.

A single and flat interface between a metal and a dielectric is referred to as the simplest form of SPP in terms of geometry. Specifically, assuming that the SPPs wave propagates along the x-direction with a wavevector β, then $\frac{\partial}{\partial x} = i\beta$, and that the structure is purely 2-dimensional that is there is no spatial variation along the y-direction, then $\frac{\partial}{\partial x} = 0$ and so simplified form as follows [1]:

$$\frac{\partial E_y}{\partial z} = -i\omega\mu_0 H_x \tag{2.36a}$$

$$\frac{\partial E_x}{\partial z} - i\beta E_z = i\omega\mu_0 H_y \tag{2.36b}$$

$$i\beta E_y = i\omega\mu_0 H_z \tag{2.36c}$$

$$\frac{\partial H_y}{\partial z} = i\omega\varepsilon_0\varepsilon E_x \tag{2.36d}$$

$$\frac{\partial H_x}{\partial z} - i\beta H_z = -i\omega\varepsilon_0\varepsilon E_y \tag{2.36e}$$

$$i\beta H_y = -i\omega\varepsilon_0\varepsilon E_z \tag{2.36f}$$

The above equations can be clearly divided into two sets: 1) Transverse magnetic (TM) mode and 2) Transverse Electric (TE) mode. For the earlier case, the electric field components along x and z axis and magnetic field component only along the y-axis are non-zero, whereas it is vice-versa for the latter case.

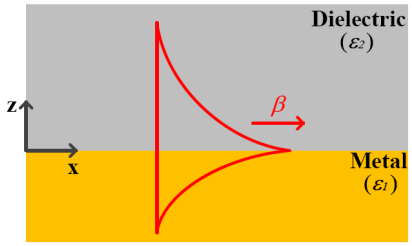

Fig 2.6. Schematic view of SPPs propagating along a single metal-dielectric interface in two dimensions [29].

For TM mode, the equations reduce to the followings:

$$\frac{\partial E_x}{\partial z} - i\beta E_z = i\omega\mu_0 H_y \tag{2.37a}$$

$$E_x = -\frac{i}{\omega\varepsilon_0\varepsilon}\frac{\partial H_y}{\partial z} \tag{2.37b}$$

$$E_z = -\frac{\beta}{\omega\varepsilon_0\varepsilon}H_y \tag{2.37c}$$

The field components can be easily found from the solutions and expressed as [30]:

For z < 0,

$$H_y(z) = A_1 e^{i\beta x} e^{k_1 z} \tag{2.37d}$$

$$E_x(z) = -\frac{iA_1 k_1}{\omega\varepsilon_0\varepsilon_1} e^{i\beta x} e^{k_1 z} \tag{2.37e}$$

$$E_z(z) = -\frac{A_1\beta}{\omega\varepsilon_0\varepsilon_1} e^{i\beta x} e^{k_1 z} \tag{2.37f}$$

For z > 0,

$$H_y(z) = A_2 e^{i\beta x} e^{-k_2 z} \tag{2.38}$$

$$E_x(z) = -\frac{iA_2k_2}{\omega\varepsilon_0\varepsilon_2} e^{i\beta x} e^{-k_2 z} \tag{2.39}$$

$$E_z(z) = -\frac{A_2\beta}{\omega\varepsilon_0\varepsilon_2} e^{i\beta x} e^{-k_2 z} \tag{2.40}$$

where $k_i^2 = \beta^2 - k_0^2\varepsilon_i$ (i=1,2) and The continuity of H_y and E_x at the boundary condition z = 0 and that leads to, $A_1 = A_2$ and $k_1\varepsilon_2 = -k_2\varepsilon_1$. As the field of SPPs is confined at the interface of metal and dielectrics, and evanescently propagates along z-axis, therefore, the condition Re [K_1] > 0 and Re [K_2] > 0 demands that Re [ε_1] < 0 if ε_2 > 0. According to [31], the condition stated before is satisfied for both the cases of infrared and visible light, it can be concluded that SPPs can exist for the TM polarization.

The dispersion relation of SPPs at a single metal-dielectric interface per equation 2.36 :

$$\beta = k_0\sqrt{\frac{\varepsilon_1\varepsilon_2}{\varepsilon_1+\varepsilon_2}} \tag{2.41}$$

Here, $k_0 = \omega/c$ is the free space wavevector, and c is the speed of light in vacuum.

For the case of TE mode, the equations 2.37 reduce to:

$$\frac{\partial H_x}{\partial z} - i\beta H_z = -i\omega\varepsilon_0\varepsilon E_y \tag{2.42a}$$

$$\frac{\partial E_y}{\partial z} = -i\omega\mu_0 H_x \tag{2.42b}$$

$$i\beta E_y = i\omega\mu_0 H_z \tag{2.42c}$$

And the field components can be written as [29]:

For z <0,

$$E_y(z) = A_3 e^{i\beta x} e^{k_1 z} \tag{2.43a}$$

$$H_x(z) = \frac{iA_3k_1}{\omega\mu_0} e^{i\beta x} e^{k_1 z} \tag{2.43b}$$

$$H_z(z) = \frac{A_3\beta}{\omega\mu_0} e^{i\beta x} e^{k_1 z} \tag{2.43c}$$

For z > 0,

$$E_y(z) = A_4 e^{i\beta x} e^{-k_2 z} \tag{2.44a}$$

$$H_x(z) = -\frac{iA_4 k_2}{\omega \mu_0} e^{i\beta x} e^{-k_2 z} \tag{2.44b}$$

$$H_z(z) = \frac{A_4 \beta}{\omega \mu_0} e^{i\beta x} e^{-k_2 z} \tag{2.44c}$$

The continuity of E_y and H_x at the boundary condition z = 0 and that leads to $A_3 = A_4$ and $k_1 = k_2$

Here it can be seen from equation 2.15 that it does not satisfy the condition of Re $[K_1] > 0$ and Re $[K_2] > 0$ as derived from the previous section. Hence, it can be concluded that SPPs cannot exist for the TE polarization.

2.8 Materials

Different materials are employed in the construction of waveguides, and SPPs can propagate along with the interfaces of a large set of materials. The materials can have positive, negative near-zero and zero permittivity and permeability. Metamaterials, metals, and dielectrics are examples of materials employed in waveguide structures and interfaces. This section covers the materials description and the calculation methods of permittivity and permeability

2.8.1 Electromagnetic material

The presence of both electric and magnetic monopoles in electromagnetic materials shas expanded the range of parameters, and their permeability and permittivity can be categorized as negative, positive, and non-zero. A magnetic monopole is considered a crucial mathematic tool and theoretically valid despite the fact that it does not exist [28]. Primitivity and permeability, those are frequency-dependent, are characterized through different models in the literature. Nonetheless, the entire range of refractive index, starting from double-positive to double negative values, should be represented through all models to demonstrate all

features of any electromagnetic materials. The Drude-Lorentz model [1] is such a model that involves the response of material after an electromagnetic field was incident, and it was found efficient in defining the susceptibilities of electromagnetic materials. Electric permittivity is the result of a material polarizing in response to an external electric field and thereby generating an internal electric field. The permittivity expression of an LHI material can be classically derived by solving the equation of motion of each electron of the form [29].

$$\sum F = m_e a = m_e \left(\frac{d^2x}{dt^2} + \Gamma_e \frac{dx}{dt} + \omega_{0_e}^2 x\right) = -q_e E(x,t) \tag{2.45}$$

in the material, for an electron of charge -e under the action of the electric field E. Here x is the displacement of the electron under the effect of E, ω_{0e} is the electric resonance frequency corresponding to the electron binding energy, Γ is a phenomenological damping constant (Γ_e refers to electric damping constant), and m_e is the mass of the electron refers to electric damping constant. Employing the solution to Eq. (2.27) along with [29]:

$$p = \epsilon_0 \chi_e E = -ex, \chi_e = \frac{\epsilon}{\epsilon_0} - 1 \tag{2.46}$$

the expression for the polarization is,

$$p = \frac{e^2}{m_e}(\omega_0^2 - \omega^2 - i\omega\Gamma_e)E \tag{2.47}$$

Polarization of materials is the sum of all individual dipoles, and for the materials with a single atom type, every electron has the same binding energy. Therefore, the permittivity of the material with *N*e electrons per unit volume has the form,

$$\frac{\epsilon(\omega)}{\epsilon_0} = 1 + \frac{F_e \omega_e^2}{\omega_{0_e}^2 - \omega^2 + i\Gamma_e \omega} \tag{2.48}$$

where *F*e is electric oscillation strength, and all F_e, $\omega_{0e,}$ and Γ_e describe charge-Ion dipole oscillation. In Eq. (2.31), ε_o is the permittivity of free space, and ω is the operating frequency. The permittivity of an EM material, which is frequency-dependent, can be expressed in the form of Drude-Lorentz through (2.31) [29]. ω denotes the angular frequency of the incident

EM field. In this equation, ω_e is the electric plasma frequency.

$$\omega_p \stackrel{\text{def}}{=} \sqrt{\frac{N_e q_e^2}{m_e \epsilon_0}} \stackrel{\text{def}}{=} \omega_e \tag{2.49}$$

where *N*e is the number density of electrons, q_e and m_e are electron charge and mass and ε_o is vacuum permittivity. Both ω_e and ω_p are used in literature for the plasma frequency. The complex refractive index of the lossy EM material is [29]

$$n \stackrel{\text{def}}{=} \sqrt{\frac{\epsilon\mu}{\epsilon_0\mu_0}} = n_r + in_i \tag{2.50}$$

As square roots have two possible solutions, one positive and one negative, the appropriate case should be chosen. For passive materials considered in this thesis, the sign that corresponds to $n_i > 0$ should be chosen to ensure that the material does not have gain. This choice leads to $n_r < 0$ at frequencies that have both $\acute{\varepsilon} < 0$, $\acute{\eta} < 0$. The behavior of a material which is consists of both electric and magnetic monopoles can be realized through another material on a large scale since the earlier material usually does not exist in nature. For example, materials that show both magnetic and electric characteristics are used to understand the existence of` magnetic monopoles.

2.8.2 Metals

Metals are considered to be a significant case of dispersive LHI materials. In this part, the electric metal's form and hypermagnetic metal are introduced. The electric metal is referred as the metal with both positive and negative permeability within the range of frequency of interest. The term "hypermagnetic metal" is simply referred to as the magnetic analogy of an electric metal. Despite the fact these types of materials do not exist, they bring the concepts of metamaterials. Since in SPPs, the propagation remains parallel to the interface, only TM mode is supported by any electric metal. In the same manner, due to the propagation of the

magnetic field being parallel, only TE mode supported for hypermagnetic materials. The above characteristics are important for SPP. However, be it electric or hypermagnetic, the aim of this paper is to characterize SPP in full fledge in the case of any material.

The combination of electric metals and hypermagnetic metal can generate an effective material with both electric and magnetic charges. Such a material can have double-positive, double-negative, ‘-negative and μ-negative refractive-indices as the incident EM field cause the oscillations of both electric and magnetic plasmas. This behavior of these materials based on the combination of electric metals and hypermagnetic metal can be in accordance with the behavior of metamaterials.

2.9 SPPs Waveguiding

Having described the basics of SPPs in section 2.6, in this section we continue to discuss the propagation properties of SPPs. Two critical parameters that determine mode characteristics are the propagation length L_p and the normalized mode area A (i.e. a larger value of A corresponds to a lower degree mode confinement) and are defined as [4]

$$L_p = \lambda/\left[4\pi \mathrm{Im}(n_{eff})\right] \tag{2.51}$$

$$A = \frac{A_m}{A_0} = \frac{\iint_{-\infty}^{\infty} W(x,y)dxdy}{\max\left[W(x,y)\right]} \times \frac{1}{A_0} \tag{2.52}$$

where λ is the operating wavelength, Im(n_{eff}) is the imaginary part of the mode effective refractive index n_{eff}, A_m is the mode area, $A_o = \lambda^2/4$ is the diffraction-limited mode area, and the energy density $W(x, y)$ is defined as [34]

$$W(x,y) = \frac{1}{2} Re\left\{\frac{d[\omega\varepsilon(x,y)]}{d\omega}\right\} |E(x,y)|^2 + \frac{1}{2}\mu_0 |H(x,y)|^2 \tag{2.53}$$

where $E(x, y)$ and $H(x,y)$ are the electric and magnetic fields, respectively.

Research on plasmonic waveguides dates back to the 1970s to 1980s. In these early works, it was found that the SPPs waveguides can be used to localize guided modes beyond the diffraction limit. Later in 1997, J. Takahara et al. firstly demonstrated the possibility of sub-diffraction guiding of SPPs modes in a cylindrical metal nanowire or nanohole configuration [35]. However, the sub-diffraction guiding of SPPs (i.e., the subwavelength mode confinement) was achieved at the cost of a short propagation length. Therefore, from the early 2000s, research interests started to focus on compromising the tradeoff between the mode confinement and propagation length [36]. In the early 2000s, two important plasmonic heterostructures were investigated, the insulator-metal-insulator (IMI) waveguide and the metal-insulator-metal (MIM) waveguide. The IMI waveguide can guide SPPs over distances of several centimeters, but the associated EM fields are weakly confined. While the MIM waveguide exhibits subwavelength mode confinement, it has a large attenuation loss, leading to a propagation length that is only in the order of a micrometer or lower. In the years that followed, various types of SPPs waveguides were proposed to mitigate this tradeoff, which included a metal wedge waveguide, a metal V-groove waveguide, and a dielectric-loaded SPPs (DLSPPs) waveguide. It was found that the metal wedge and V-groove waveguides can realize subwavelength confinement and an acceptable propagation length up to tens of micrometers. While the DLSPPs waveguide possesses an increased propagation length (up to hundreds of micrometers) it does have a relatively larger mode area. The tradeoff remained challenging until 2008 when there was a proposal for a novel hybrid SPPs (HSPPs) waveguide by R. F. Oulton [35], which could simultaneously offer subwavelength mode confinement and an extended propagation length up to hundreds of micrometers. This breakthrough research opened the way recently to a new range of SPPs based applications, such as a nanolaser and nanotweezers [39].

2.9.1 Dielectric loaded SPPs (DLSPPs) waveguide

A DLSPPs waveguide is one of the most popular plasmonic waveguides investigated in recent years. Fig. 2.7 shows a schematic view of the DLSPPs planar waveguide. Compared to a single planar dielectric-metal waveguide, a higher permittivity dielectric_1 layer is introduced in the DLSPPs waveguide, i.e. $\varepsilon_2 > \varepsilon_3$, with a thickness d.

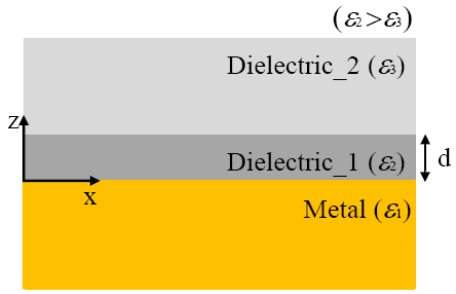

Fig. 2.7: Geometry of the 2D-DLSPPs waveguide with no permittivity variation along the y-direction [29]

To investigate DLSPPs waveguide, it is assumed that SPPs propagate long the x-direction, and there is no spatial variation along the y-direction. Then the magnetic field H_y can be expressed as follows [36]:

$$H_y(z) = Ae^{k_1 z}e^{i\beta x}, \quad z < 0 \tag{2.54a}$$

$$H_y(z) = Be^{i\beta x}e^{k_2(z-d)} + Ce^{i\beta x}e^{-k_2 z}, \quad 0 < z < d \tag{2.54b}$$

$$H_y(z) = De^{i\beta x}e^{k_3(z-d)}, \quad z > d \tag{2.54c}$$

and $E_x(z)$ and $E_z(z)$ are given by eq. (2.22a) and eq. (2.22b), respectively, in which

$$k_i^2 = \beta^2 - k_0^2\varepsilon_i \quad (i = 1,2,3) \tag{2.55}$$

By applying the boundary conditions, i.e. the continuity of H_y and E_x at the boundary $z = 0$ and $z = d$, the dispersion relation of the DLSPPs mode can be expressed as [37]:

$$tanhd = \frac{\varepsilon_1 k(\varepsilon_2\theta + \varepsilon_3\gamma)}{\varepsilon_2\varepsilon_3 k^2 - \varepsilon_1^2\gamma\theta} \tag{2.56a}$$

where

$$\gamma = \sqrt{\beta^2 - k_0^2\varepsilon_2} \tag{2.56b}$$

$$\theta = \sqrt{\beta^2 - k_0^2 \varepsilon_3} \tag{2.56c}$$

$$k = \sqrt{k_0^2 \varepsilon_1 - \beta^2} \tag{2.56d}$$

For the DLSPPs waveguide with a very thick dielectric_1 layer, it can be speculated that the DLSPPs mode is actually the SPPs mode propagating along the single dielectric_1-metal interface. As *d* decreases, the field of the DLSPPs mode will be progressively squeezed inside the dielectric_1 region, indicating an enhanced mode confinement compared to that for the case of a very thick dielectric_1 layer. However, a further decrease in *d* gives rise to a rapid increase in the field outside the dielectric_1, corresponding to a weaker mode confinement. This implies that there is an optimal value of *d*, at which the DLSPPs mode achieves the strongest mode confinement. It has been demonstrated that a DLSPPs waveguide can provide a modest mode confinement ($A \sim 0.16\lambda_2$) as well as a relatively long propagation length (L_p ~ 100 μm) [37].

2.9.2 Hybrid SPPs (HSPPs) waveguide

The schematic diagram of a typical HSPPs waveguide is shown in Fig. 2.9. Compared to DLSPPs waveguide, a lower permittivity dielectric_2 (ε_3, with a thickness of *d*) is sandwiched between the metal substrate and the higher permittivity dielectric_1 (ε_2, with a thickness of *h*).

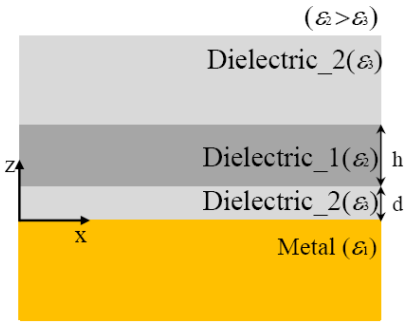

Fig. 2.8: Geometry of the HSPPs waveguide with no permittivity variation along the y-direction [37].

To investigate the properties of the HSPPs waveguide, it is assumed that SPPs propagate

along the *x*-direction and there is no spatial variation along the *y*-direction. Then the magnetic field H_y can be expressed as follows [37]:

$$H_y(z) = Ae^{k_1 z}e^{i\beta x}, \quad z < 0 \tag{2.57a}$$

$$H_y(z) = Be^{i\beta x}e^{k_2(z-d)} + Ce^{i\beta x}e^{-k_2 z}, \ 0 < z < d \tag{2.57b}$$

$$H_y(z) = De^{i\beta x}e^{k_3(z-d-h)} + Ee^{i\beta x}e^{-k_3(z-d)}, \ d < z < (d+h) \tag{2.57c}$$

$$H_y(z) = Fe^{i\beta x}e^{k_2(z-d-h)}, z > (d+h) \tag{2.57d}$$

and $E_x(z)$ and $E_z(z)$ are given by eq. (2.57a) and eq. (2.57b), respectively, in which

$$k_i^2 = \beta^2 - k_0^2\varepsilon_i \qquad (i = 1,2,3) \tag{2.58}$$

By applying the boundary conditions i.e. the continuity of H_y and E_x at the boundary $z = 0$, $z = d$, and $z = (d+h)$, the dispersion relation of the HSPPs mode can be expressed as :

$$\frac{k_1}{\varepsilon_1}m_{11} + \frac{k_2}{\varepsilon_2}m_{22} - m_{21} - \frac{k_1 k_2}{\varepsilon_1\varepsilon_2}m_{12} = 0 \tag{2.59}$$

where, m_{11}, m_{12}, m_{21} and m_{22} are given by,

$$\begin{bmatrix} m_{11} & m_{12} \\ m_{21} & m_{22} \end{bmatrix} = \begin{bmatrix} \cos(k_2 d) & -\frac{\varepsilon_2}{k_2}\sin(k_2 d) \\ \frac{k_2}{\varepsilon_2}\sin(k_2 d) & \cos(k_2 d) \end{bmatrix} \times \begin{bmatrix} \cos(k_3 h) & -\frac{\varepsilon_3}{k_3}\sin(k_3 h) \\ \frac{k_3}{\varepsilon_3}\sin(k_3 h) & \cos(k_3 h) \end{bmatrix} \tag{2.60}$$

Eq. (2.60) can offer accurate solutions for the HSPPs mode; however, the physical explanation of the HSPPs mode from eq. (2.60) is not straightforward. The physical explanation can be provided by the so-called coupled-mode theory. In this theory, it is believed that HSPPs mode is generated due to the coupling between the photonic waveguide mode (supported by the dielectric_1 layer) and the SPPs mode (excited at the single dielectric_2-metal interface). In other words, the dielectric_1 surrounded by the dielectric_2 can support a dielectric waveguide mode, and the dielectric_2-metal interface can support a SPPs mode. When the two modes with similar effective refractive indices are brought close

to each other, the dielectric waveguide mode will couple with the SPPs mode and form a HSPPs mode. Recently the HSPPs waveguide has attracted significant interest because it possesses a confinement capability beyond the diffraction limit ($A \sim \lambda^2/400$ while retaining a relatively long propagation length ($L_p \sim 150$ μm [38]).

2.10 Conclusion

Overall, then as discussed in the sub-sections above, a variety of SPPs waveguide types have been developed. Each has its own strength and weakness, and still retains the fundamental tradeoff between the mode confinement and propagation length. The choice of SPPs waveguiding schemes should be selected by the requirements of specific applications.

Chapter 3

ANALYSIS TECHNIQUES

3.1 Introduction

This chapter narrates the prevalent simulation software COMSOL Multiphysics^{TM} which was used to analyze the characteristics of Long-Range Surface Plasmon Polariton effect in different types of waveguides. COMSOL Multiphysics^{TM} is based on the finite element method, which breaks the overall simulation area into small domains and evaluates the total field values by summing each of them. Also, the Partial differential equations are discussed in this section. These PDEs are used to evaluate the different parameters after defining the proper boundary conditions as per the analysis domain. And last but not least, the meshing techniques is stated that play a significant role to distribute the simulation domain as per the requirement of the different structure, materials, and distribution of fields.

3.2 The Finite Element Analysis and COMSOL Multiphysics

The finite element method can offer an approximate solution to a particular problem integrating partial differential equations. The civil engineers initially used this method to analyze stress in the structures. Later finite element method was used in several other disciplines of engineering and considered as a key tool to model the various scientific problems- such as electric and magnetic fields, energy distribution over the area, and others. Engineers can apply this finite element method on the models with complex structures and eccentric boundary conditions, which made it extremely popular among the academics and field engineers.

To imply the finite element method on the particular geometry leads to discretize or divide the whole structure into a finite number of smaller elements. This smaller unit is much easier

to analyze than that of the entire model area for its more superficial properties. Thus, several meshes from the overall geometry are formed by joining the smaller units, named as vertices. The unknown field profile for these small units can be sought and approximated using simple smooth functions such as polynomials, called interpolation or shape functions. Thus, the field parameters can be given by [39]

$$\phi = N_1\phi_1 + N_2\phi_2 + \cdots + N_m\phi_m \tag{3.1}$$

where the unknown filed is given by ϕ_i for the interpolation function N_i for each element. Finite elements with linear interpolation functions give exact values for ϕ_i if the result being sought is quadratic, quadratic elements give similar values for ϕ_i for cubic solutions, etc. The accuracy of the solution solely depends on the distribution of the elements. The result tends to get more accurate with the larger number of meshes, but the requirements of processing resources will be higher. So, the distribution of mesh is rather not symmetric over the entire geometry rather finer than other areas where the precision of the result is critical for the calculation. A matrix equation can be got, which controls the comportment of finite elements for a specific problem applying suitable assumption. This resultant characteristic equation has different names as per the field of study: in the optical module, it is called the refractive index matrix. The weighted residual method is a way of originating this characteristic matrix, while the variational method can also be useful.

For the problems that work with the depreciation of any functional, the variational method is beneficial. It can be said that Hamilton's principle works with such kind where the full energy of a system is defined. On the other hand, the variational method is used on problem which is related to the variational principle. Similarly, when the problem is related to differential equations, the weighted residual method is mainly used. The motto is to minimize the

remaining after a rough or test solution is replaced to the differential equations [39], and are universal mathematical tools applicable to solve all types of PDEs. Galerkin method is the most commonly used variational method [39].

From the characteristics matrices, set linear simultaneous equations can be got for the entire problem domain. After solving these equations, we got the mandatory field at the vertices, ϕ_i, adding up all the field quantities from the small meshes. The necessary boundary conditions and initial conditions should be appropriately set before executing the solution. To work with a sparse and symmetric matrix, we have to invert it to get the accurate results. The direct and iterative method is the two different techniques used to solve simultaneous equations [39]. To use the direct method, the set of equations should be entirely amassed before beginning, and it is based on well-known Gauss elimination and LU decomposition methods. The problem associated with a large number of mesh vertices requires massive storage. Iterative methods work efficiently for bigger models, such as the Gauss-Deidel method. They are implied to avoid the total accumulation of matrices of a large system [39].

Many commercial software offers automation of finite element simulations, and COMSOL Multiphysics is very popular among them[45]. COMSOL Multiphysics gives a user-friendly environment for geometric modeling and a large material database. COMSOL Multiphysics enables a person to evaluate the desired field, having very brief knowledge of PDEs or numerical analysis through in-build interfaces. COMSOL allows an engineer to express their PDEs by coefficients, in the weak form, or a general form. COMSOL introduces numerous modules useful to calculate different parameters, like the heat transfer module, the acoustics module, chemical engineering module, Optical module, etc. Each module contains the differential equations, which can be used to evaluate the diverse field parameters conveniently. As long as this research work is related to the optical modes of different

waveguides and how different characterizing parameters of the waveguides can be realized as active devices, COMSOL only uses the optical module, and later we strictly discuss on this topic.

Firstly, engineers use some computer-aided design utilities to define the structure of any specific models in COMSOL. Later, from the vast material database, the particular material characteristics such as permittivity, density, and the refractive index can be given with utmost ease. These material parameters and related equations for different materials are emblazoned in COMSOL that allows the user to describe the problem scenario very quickly. Lastly, after applying the necessary boundary condition, the model area is discretized with small finite elements according to any suitable algorithm to solve the PDEs.

3.3 Boundary Conditions of PDEs

The relevant partial differential equations generated from Maxwell's equations should be solved while investigating the optical modes of metal waveguides with variation in operating frequencies. Each of these equations is associated with a set of boundary conditions.

3.3.1 Eigenmode analysis

2D eigenmode solver of COMSOL belongs to the optical module calculates the mode field *F(x, y)* of a wave propagating in the z-direction deals with following Maxwell's curl equations

$$\nabla \times \nabla \times \boldsymbol{E} - \tilde{n}^2(x,y)k_0^2\boldsymbol{E} = 0 \tag{3.2}$$

$$\nabla \times \tilde{n}^{-2}(x,y)\nabla \times \boldsymbol{H} - k_0^2\boldsymbol{H} = 0 \tag{3.3}$$

where, $\boldsymbol{H} = \boldsymbol{H}(x,y)e^{i(\beta z-\omega t)}$, $\boldsymbol{E} = \boldsymbol{E}(x,y)e^{i(\beta z-\omega t)}$, $k_0^2 = \omega^2\mu_0\epsilon_0$ and β is the propagation constant in the **z-**direction. COMSOL's optical module provides many supplementary boundary conditions which simplify the modeling process along with general boundary

conditions that always have to be fulfilled in electromagnetic theory. These consist of environments that permit the boundaries to act like perfect electric or magnetic conductors (i.e. $n \times E = 0$, or $n \times H = 0$), and the perfectly matched layer (PML). A perfectly matched layer acts both as a boundary condition and a surplus domain that captivates the radiation incident on a surface area without creating any reflections [45]. In this research work, the perfectly matched layer conditions are used which is related to two further conditions - the scattering and impedance boundary conditions.

3.4 Discretization

The most important part of the simulation process is the meshing of a model. The geometry of the structure does not control the result of the partial differential equations itself but the discretization of the analysis domain. Only a suitable discretization should not be sufficient enough to solve all the essential aspects of the resolution in detail. Also, optimizing the meshing algorithm is equally crucial to saving the computer's resources during the simulation process. COMSOL provides an automatic discretization facility like any other finite element analysis software, which usually works fine. As stripe waveguides possess the extreme aspect ratio of plasmonic (nanometer or micrometer level), the automatic meshing algorithms are not enough. The reason is automated meshing algorithms do not consider the crucially of field calculation in particular regions. The user must optimize how the mesh should be generated. Still, the number of meshes must ensure that LR-SPP modes typically extend several μm into the cladding away from the metal waveguides.

There are two types of meshes - free mesh and mapped mesh commonly. Free meshes consist of triangular and tetrahedral elements in two-dimensional models and three-dimensional models, respectively. Similarly, mapped meshes contain quadrilateral and hexahedral elements segments, respectively. The free mesh is created by a triangulation method called

the Delauney algorithm, thus functional for each dimension [45]. This triangulation method is applicable for every geometry of different shape or topology, making the free mesh advantageous over others. On the other hand, the use of mapped mesh is limited to regular mesh geometries that are mostly rectangular. The geometry of the model can be changed to meet the requirements of perfect meshing strategy.

COMSOL makes mapped meshes governed by an algorithm to outline a consistent square grid and then relates to the model using transfinite interpolation [45]. The types of mapped mesh are not dependent on a set of tunable parameters that differs from the free mesh. Two types of meshes are exhibited in fig. 3.1.

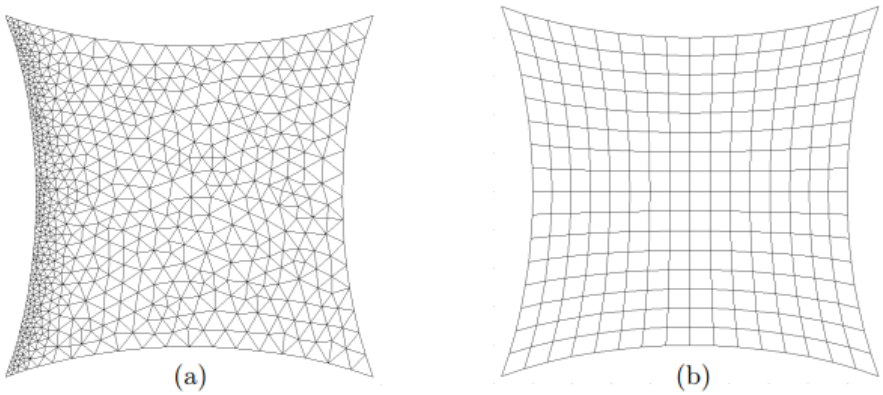

Fig. 3.1: (a) A triangular mesh with a denser area in the left side. (b) A quadrilateral mesh of evenly distributed region.

The boundaries of different domains of a specific model usually are divided into small segments based on the quantity of elements and the orientation of the vertices both types of meshes. To ensure the better tuning of the discretization from users, subdomains mesh elements are kept into fixed points. A similar example is shown in Fig 3.1a, where the mesh seems finer at the left region, keeping the number of segments 70. When modeling plasmonic stripe waveguides, this feature is quite useful because, in the stripe region, the number of the mesh can be varied manually as per user requirements. Almost in every case in this research, the phenomenon of the LRSPP modes on the waveguide model was analyzed. The mesh of

a fixed density was defined in the waveguide to introduce a uniformity among various structures, which makes the comparative study more reliable. Fig. 3.2 exhibits a commonly used meshing for stripe waveguide. Here the metal stripe is discretized to maintain a specific vertex spacing in the lateral and transverse direction.

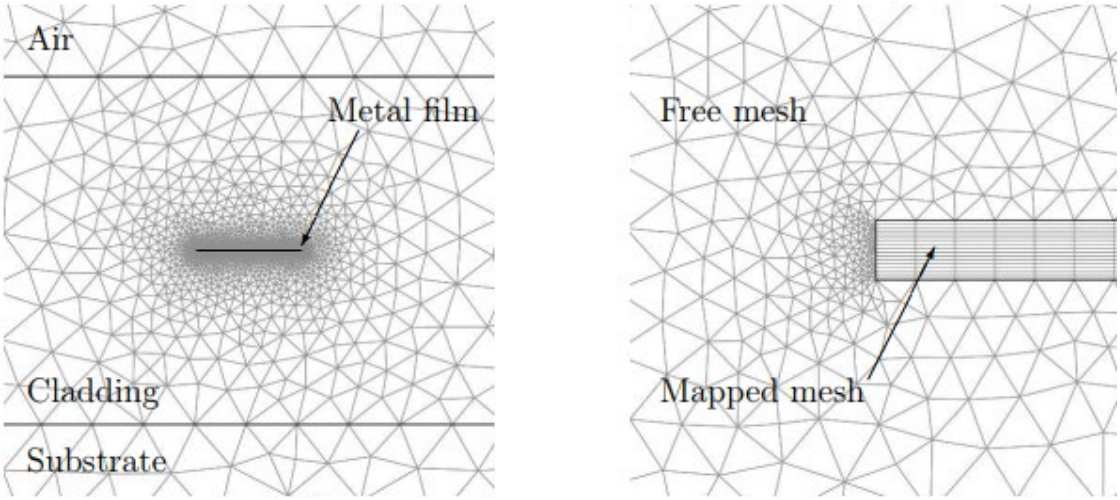

(a) (b)

Fig. 3.2: (a) The meshed model of a stripe waveguide (b) Mapped mesh, which was defined manually in metal strip, enclosed by a free mesh in area of cladding . Here, the thickness of the metal is 13 nm [45].

3.5 Surface Plasmon Polaritons Restricted to Single Interface

The simplest geometry supporting Surface Plasmon polaritons (SPPs) is that it contains only a single and flat interface. In this chapter, we analyze this simple structure theoretically and show some simulations that verify the result.

3.5.1 Theoretical analysis

Fig. 3.1 shows an interface between a dielectric, non-absorbing half-space ($y>0$) with a real dielectric constant ε_2 greater than zero, and another conducting half-space ($y<0$) having a

dielectric function $\varepsilon_1(\omega)$. The necessity of a metallic area implies that $\mathrm{Re}[\varepsilon_1] < 0$. For metals, the overall condition is fulfilled at a frequency below the bulk plasmon frequency ω_p.

As, $k_x = 0$ from $k_0^2\varepsilon = k_y^2 + k_z^2$, for evanescent decay in the perpendicular y-direction k_y needs to be imaginary. So, $k_z^2 - k_0^2\varepsilon = \beta^2 - k_0^2\varepsilon > 0$. Let, k_1 , k_2 are the wave vector along y axis for y<0 and y>0, respectively.

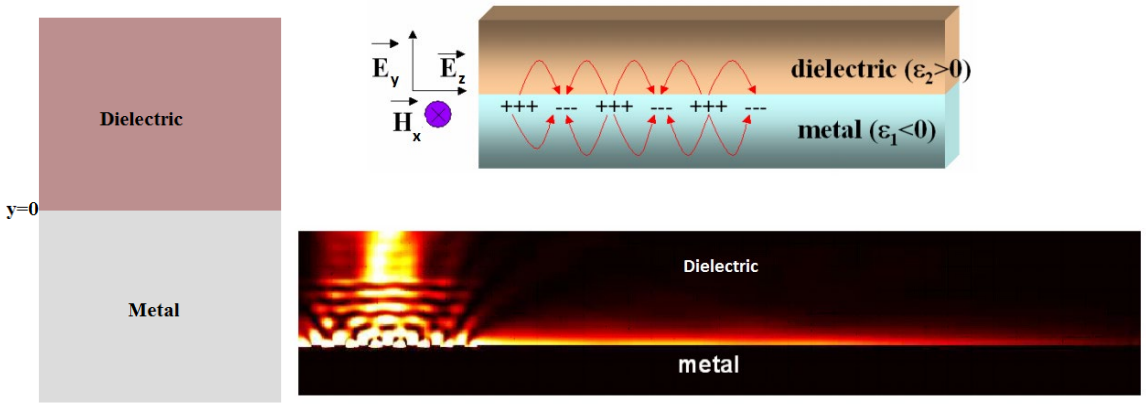

Fig. 3.3: Surface-plasmons on dielectric-metal boundaries.

For TM results:

Using the equations towards half spaces, both yields:

for y>0

$$H_x(y) = A_2\, e^{-i\beta z}\, e^{-k_2 y} \tag{3.4a}$$

$$E_y(y) = -\frac{\beta}{\omega\varepsilon_0\varepsilon_2} A_2\, e^{-i\beta z}\, e^{-k_2 y} \tag{3.4b}$$

$$E_z(y) = \frac{i(-k_2)}{\omega\varepsilon_0\varepsilon_2} A_2\, e^{-i\beta z} e^{-k_2 y} \tag{3.4c}$$

for y<0

$$H_x(y) = A_1\, e^{-i\beta z} e^{k_1 y} \tag{3.5a}$$

$$E_y(\mathrm{y}) = -\frac{\beta}{\omega\varepsilon_0\varepsilon_1}\mathrm{A}_1\, e^{-i\beta z} e^{k_1 y} \tag{3.5b}$$

$$E_z(\mathrm{y}) = \frac{i(k_1)}{\omega\varepsilon_0\varepsilon_1}\mathrm{A}_1\, e^{-i\beta z} e^{k_1 y} \tag{3.5c}$$

where, A_1 and A_2 are constants and

$$k_1^2 = \beta^2 - k_0^2\varepsilon_1 \tag{3.6a}$$

$$k_2^2 = \beta^2 - k_0^2\varepsilon_2 \tag{3.6b}$$

When the operating frequency is lower than the plasmon frequency of the metal, ε_1 holds negative value, and the argument of the square root will always satisfy the below condition $\beta^2 - k_0^2\varepsilon > 0$. Continuity of H_x at y = 0 implies that A_1=A_2 and continuity of E_z at the interface supports

$$\frac{k_2}{\varepsilon_2} = -\frac{k_1}{\varepsilon_1} \tag{3.7}$$

After the universal convention in the polarity of the exp in (3.4,3.5), confinement towards the surface needs that Re[ε_1]<0 if ε_2>0 - the surface waves remain only at edges between a metal with the inverse polarity of the dielectric permittivity (Real part) of respective materials, i.e., between an insulator and a conductor. From (3.6) and (3.7)

$$k_2^2 = k_1^2\left(\frac{\varepsilon_2}{\varepsilon_1}\right)^2 = (\beta^2 - k_0^2\varepsilon_1)\left(\frac{\varepsilon_2}{\varepsilon_1}\right)^2 = \beta^2 - \mathrm{k}_0^2\,\varepsilon_2$$

$$\varepsilon_2^2(\beta^2 - k_0^2\varepsilon_1) = \varepsilon_1^2(\beta^2 - \mathrm{k}_0^2\,\varepsilon_2)$$

$$\beta^2(\varepsilon_2^2 - \varepsilon_1^2) = k_0^2\varepsilon_1\varepsilon_2(\varepsilon_1 - \varepsilon_2)$$

$$\beta^2 = \frac{k_0^2\varepsilon_1\varepsilon_2}{\varepsilon_1 + \varepsilon_2}$$

$$\beta = k_0 \sqrt{\frac{\varepsilon_1 \varepsilon_2}{\varepsilon_1 + \varepsilon_2}} \tag{3.8}$$

where, $\beta = k_z = \frac{\omega}{c} \sqrt{\frac{\varepsilon_1 \varepsilon_2}{\varepsilon_1 + \varepsilon_2}}$ is the Surface Plasmon dispersion relation for a single interface.

Dispersion curve:

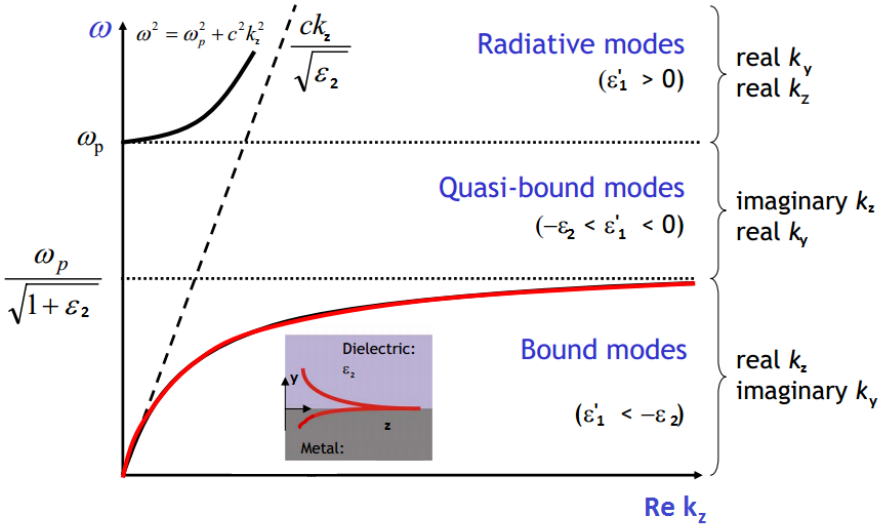

Fig. 3.4: Dispersion curve for a single interface.

Fig 3.4 shows plots of equation (3.8) i.e. dispersion relation for a single interface where the metal-dielectric junction has negligible damping and is described by the real Drude dielectric function.

In the frequency range $\omega < \omega_p$, metal dielectric constant $\varepsilon_1(\omega) < 0$, which fulfills the assumption $\beta^2 - k_0^2 \varepsilon > 0$.

Again, $$\beta = k_0 \sqrt{\frac{\varepsilon_1 \varepsilon_2}{\varepsilon_1 + \varepsilon_2}} = k_0 \sqrt{\varepsilon_2} \sqrt{\frac{\varepsilon_1}{\varepsilon_1 + \varepsilon_2}} \tag{3.9}$$

Since, ε_1 is negative, for β to be real $\varepsilon_1 + \varepsilon_2$ has to be negative. So, it can be seen that the value of the metal permittivity is required to be larger than dielectric permittivity for the SP to propagate along the interface i.e. $|\varepsilon_1| > \varepsilon_2$.

With the imposed conditions, it is also important to note that the second square root on the RHS of equation (3.9) is inevitably larger than one. So, $\beta > k_0\sqrt{\varepsilon_2}$ and this implies that the SPP excitations are always linked to the curves lying below of respective light lines. The phase-matching techniques are therefore required to excite them. [32]

Radiation into the metal happens in the transparency region where $\omega > \omega_p$. This radiation mode is called Brewster mode. Between the regime of the bound and radiative modes, a frequency gap region with purely imaginary β prohibiting propagation exists. In this region, called plasmon bandgap, the wave is evanescent, and it reflects back to the dielectric.

For small wave vectors linked to low (mid-infrared or lower) frequencies [40], the SPP propagation constant is almost equal to k_0 at the light line, and the waves spread over many wavelengths into the dielectric space. In this regime, SPPs, therefore, obtain the nature of a grazing-incidence light field and named as Sommerfeld-Zenneck waves [32]. The upper limit of frequency for propagating mode is defined as the surface plasmon frequency in which β diverges. It happens when the permittivity of the metal (ε_1) nulls the other dielectric (ε_2)

$$\varepsilon_1 = -\varepsilon_2 \Rightarrow \omega_{sp} = \frac{\omega_p}{\sqrt{1+\varepsilon_2}} \tag{3.10}$$

In this case, $v_g = \frac{d\omega}{d\beta} \to 0$. The mode thus acquires electrostatic character, and is known as the surface plasmon. This equation tells us that the surface plasmon frequency is lower with the higher index of refraction of the dielectric. Below this frequency, light propagates in a bound mode. This high confinement of light at the interface specifies a true surface mode, called Fano mode [33].

However, in real metals, $\varepsilon_1(\omega)$ is complex, as well as SPP propagation constant β. The traveling SPPs are damped with an energy attenuation length (also called propagation length).

At surface plasmon frequency ω_{sp}, the wave vector approaches a maximum, finite value, instead of having something close to infinity for the case of undamped SPP.

The propagation length can be described as the distance the wave travels along the interface until its energy falling-off to e^{-1}(≈0.368) of its real value. As the energy is directly proportional to the square of the field (energy $\propto |H|^2 \propto e^{-2\,\mathrm{Im}(\beta)z}$) , the propagation length ,

$$L_p = \frac{1}{2\,\mathrm{Im}(\beta)} \tag{3.11}$$

Fig. 3.5 shows the dispersion relation of SPPs propagating at the interface of silver/air and silver/silica, with the dielectric function $\varepsilon_1(\omega)$ of silver [19]. Also in contrast to the case of ideal metal, the region between ω_{sp} and ω_p is not prohibited any more, rather a quasi-bound leaky part of Re[β] exists in this regime.

TE surface modes:

Using the respective expressions for the field components for TE mode and continuity of H_x and E_z at the interface leads to the condition $A_1(k_1 + k_2) = 0$. As confinement to the surface

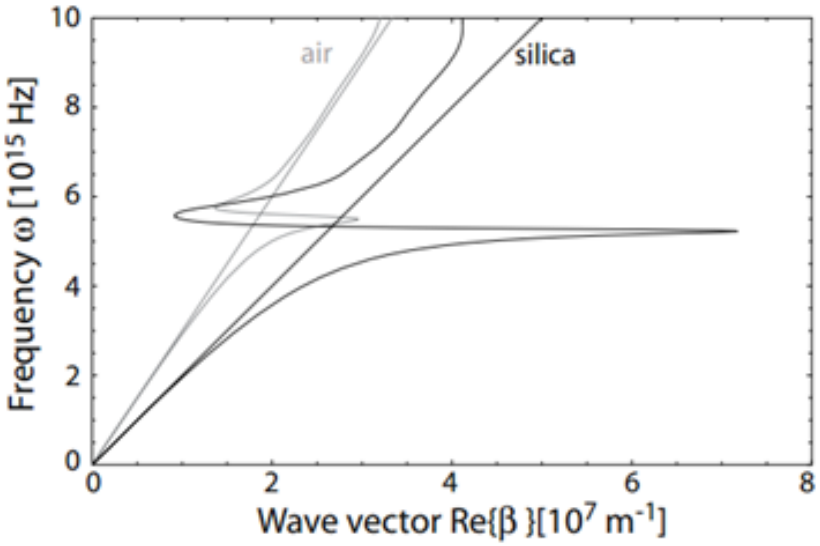

Fig. 3.5: Dispersion relation of Ag/Air (gray curve) and Ag/Si (black curve) interface.

requires Re[k_1] >0 and Re[k_2] >0, thus this condition is only satisfied if A_1 =0, and which makes A_2 =0. Thus, no surface modes exist for TE polarization. Surface plasmon polaritons only exist for TM polarization.

3.5.2 Simulation by COMSOL Multiphysics

COMSOL Multiphysics [45] (a commercial FEM based simulation software) is used to simulate the structure of a single, flat interface between a dielectric, non-absorbing half-space (y>0) with dielectric constant ε_2 =12.25 and an adjacent conducting half-space (y<0) of silver whose dielectric constant is taken from the result of Johnson and Christy [34]. The right and the left boundary is set as Perfect Magnetic Conductor (PMC) while the upper and lower boundary (which are sufficiently far so that field decays to a very low value before reaching them) is set as Scattering Boundary Condition (SBC)

Field Profile

The three principal field components (E_z, H_x, E_y) are shown in Fig. 3.6

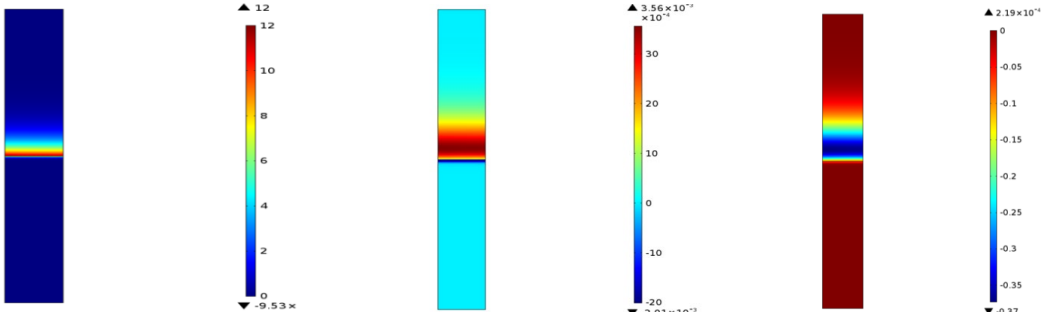

(a) (b) (c)

Fig. 3.6: E_z (a), H_x(b), E_y(c) field profile for semi-infinite metal dielectric interface obtained by COMSOL.

Dispersion Curve

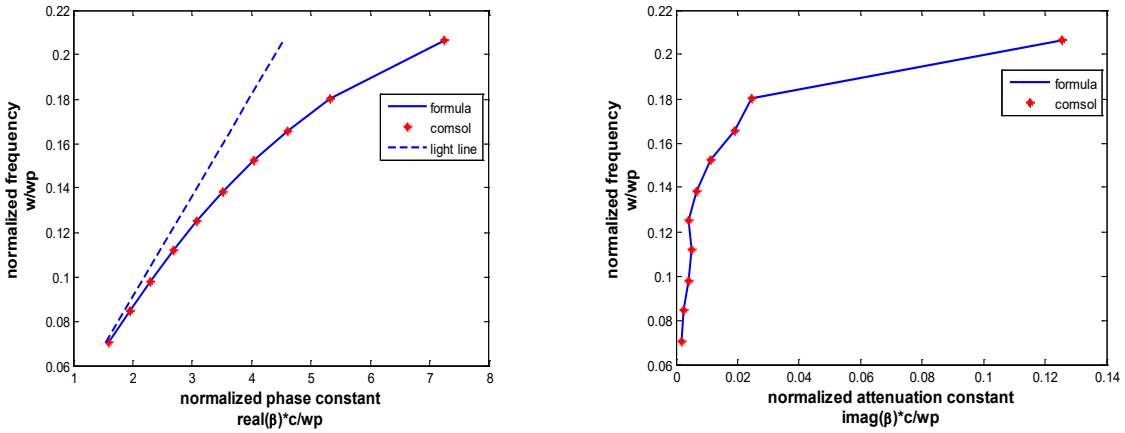

(a) real part (b) imaginary part

Fig. 3.7: Comparison of theoretical and experimental values (continuous blue line) and COMSOLresult (red asterisk) of real & imaginary part of propagation constant β .Also light line for dielectric is shown (as dashed blue line).

FEM requires a finite domain that does not accurately correspond to the semi-infinite structure assumed in theory. So the result obtained by COMSOL is not strictly compatible with the theoretical value. The value of H_z, E_x, and H_y though very small, is not equal to zero as suggested by theory. Also, the peak value of H_x and E_y occur just not at the metal interface.

3.6 Surface Plasmon Polaritons at a Thin Layer

Now we can analyze when a second interface is added to the system capable of generating SPP. It was seen that when the separation between the interfaces becomes small, the Surface Plasmons on every edge begin to correlate, turning the values of coupled modes higher with numerous fascinating characteristics.

3.6.1 Theoretical Analysis

The actual geometry of a thin layer (medium 2) between two media (1 and 3) is presented in

Fig 3.8. As previously discussed for an IM geometry, only TM-polarized wave can excite SPP in naturally-occurring materials. This statement is also valid for other geometries.

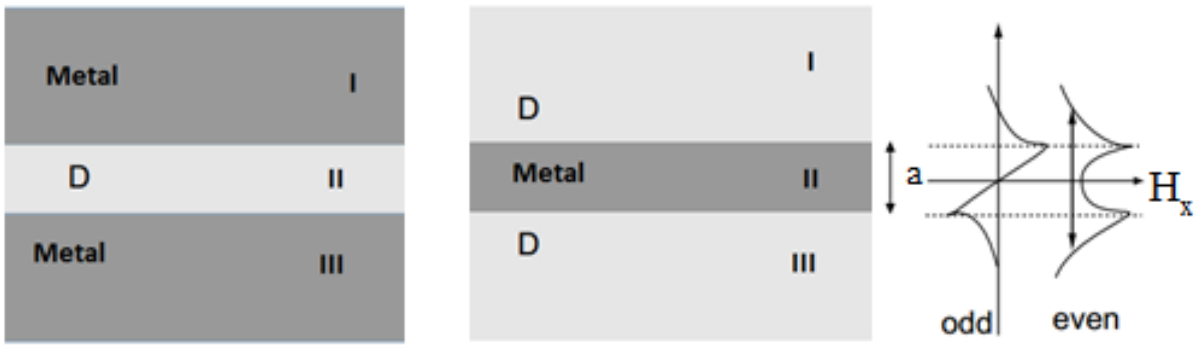

Fig. 3.8: Planar thin layer geometry.

For the theoretical purpose, equations for the lowest-order bound modes for IMI structure are investigated. So we start with a general description of TM modes that are non-oscillatory in the y-direction normal to the interfaces. Thus, we can see that the fields decay exponentially in the claddings (I) and (III). We denote the component of the wave vector perpendicular to the interfaces simply as $k_i \equiv k_{y,i}$. In the core region $-a/2<y<a/2$, the modes are restricted to the bottom and top interface of the couple. The field components are given in Table 3.1

Table 3.1: Field components at different regions for a thin layer structure

Field components	Region 1 (y>a/2)	Region 2 (-a/2< y<a/2)	Region 3 (y<-a/2)
$H_x(y)$	$Ae^{-i\beta z}e^{-k_1 y}$	$Ce^{-i\beta z}e^{k_2 y}+De^{-i\beta z}e^{-k_2 y}$	$Be^{-i\beta z}e^{k_3 y}$
$E_y(y)$	$-A\frac{\beta}{\omega\varepsilon_0\varepsilon_1}e^{-i\beta z}e^{-k_1 y}$	$-C\frac{\beta}{\omega\varepsilon_0\varepsilon_2}e^{-i\beta z}e^{k_2 y}-D\frac{\beta}{\omega\varepsilon_0\varepsilon_2}e^{-i\beta z}e^{-k_2 y}$	$-B\frac{\beta}{\omega\varepsilon_0\varepsilon_3}e^{-i\beta z}e^{k_3 y}$
$E_z(y)$	$iA\frac{(-k_1)}{\omega\varepsilon_0\varepsilon_1}e^{-i\beta z}e^{-k_1 y}$	$iC\frac{(k_2)}{\omega\varepsilon_0\varepsilon_2}e^{-i\beta z}e^{k_2 y}+iD\frac{(-k_2)}{\omega\varepsilon_0\varepsilon_2}e^{-i\beta z}e^{-k_2 y}$	$iB\frac{k_3}{\omega\varepsilon_0\varepsilon_3}e^{-i\beta z}e^{k_3 y}$

The requirement of continuity of E_z and H_x at the interface leads to:

At $y = a/2$:

$$Ae^{-k_1(a/2)} = Ce^{k_2(a/2)} + De^{-k_2(a/2)} \tag{3.12a}$$

And $$\frac{A}{\varepsilon_1}k_1e^{-k_1(a/2)} = -\frac{C}{\varepsilon_2}k_2e^{k_2(a/2)} + \frac{D}{\varepsilon_2}k_2e^{-k_2(a/2)} \tag{3.12b}$$

At $y = -a/2$:

$$Be^{k_3(-a/2)} = Ce^{k_2(-a/2)} + De^{-k_2(-a/2)} \tag{3.13a}$$

$$\frac{B}{\varepsilon_3}k_3e^{k_3(-a/2)} = \frac{C}{\varepsilon_2}k_2e^{k_2(-a/2)} - \frac{D}{\varepsilon_2}k_2e^{-k_2(-a/2)} \tag{3.13b}$$

H_x further has to fulfill the wave equation (3.15) in the three distinct regions, via

$$k_i^2 = \beta^2 - k_0^2\varepsilon_i \text{, for i =1, 2, 3.} \tag{3.14a}$$

To simplify the notation, let's define: $$R_i = \frac{k_i}{\varepsilon_i} \tag{3.15}$$

Substituting the value of $Ae^{-k_1(a/2)}$ from equation (3.12a) to (3.12b) we obtain:

$$R_1(Ce^{k_2(a/2)} + De^{-k_2(a/2)}) = R_2(-Ce^{k_2(a/2)} + De^{-k_2(a/2)})$$

multiplying by $e^{k_2(a/2)}$:

$$R_2(D - Ce^{k_2a}) = R_1(Ce^{k_2a} + D) \tag{3.16a}$$

Similarly, from (3.15) and (3.16a) we get,

$$R_2(C - De^{k_2a}) = R_3(C + De^{k_2a}) \tag{3.16b}$$

Re-arranging the terms, we can obtain the following relationship in a matrix form:

$$\begin{pmatrix} e^{k_2a}(R_1 + R_2) & R_1 - R_2 \\ R_3 - R_2 & e^{k_2a}(R_3 + R_2) \end{pmatrix}\begin{pmatrix} C \\ D \end{pmatrix} = \begin{pmatrix} 0 \\ 0 \end{pmatrix}$$

This is a homogeneous system of linear equations. Its non-zero solutions occur when the determinant of the matrix of coefficients is zero, resulting in the dispersion relation for a thin layer:

$$e^{2k_2a} = \frac{R_1-R_2}{R_1+R_2}\frac{R_3-R_2}{R_3+R_2} \tag{3.17}$$

$$e^{2k_2a} = \frac{k_1/\varepsilon_1 - k_2/\varepsilon_2}{k_1/\varepsilon_1 + k_2/\varepsilon_2}\frac{k_3/\varepsilon_3 - k_2/\varepsilon_2}{k_3/\varepsilon_3 + k_2/\varepsilon_2} \tag{3.18}$$

Symmetric structures:

For symmetric structures, media 1 and 3 are built by the same material. The dispersion relation as stated in (3.18) becomes

$$e^{2k_2a} = \left(\frac{R_1 - R_2}{R_1 + R_2}\right)^2$$

$$e^{k_2a} = \pm\left(\frac{R_1 - R_2}{R_1 + R_2}\right)$$

Which is reduced to $$\frac{R_1}{R_2} = -\frac{e^{k_2a} \pm 1}{e^{k_2a} \mp 1} = -\frac{e^{k_2a/2} \pm e^{-k_2a/2}}{e^{k_2a/2} \mp e^{-k_2a/2}} \tag{3.19}$$

$$\therefore \frac{R_1}{R_2} = -\tanh\left(\frac{k_2a}{2}\right) \text{or, } \frac{R_1}{R_2} = -\coth\left(\frac{k_2a}{2}\right) \tag{3.20}$$

From (3.16a) $$\frac{R_1}{R_2} = \frac{D - Ce^{k_2a}}{Ce^{k_2a} + D} = -\frac{Ce^{k_2a} - D}{Ce^{k_2a} + D} = -\frac{e^{k_2a/2} - \frac{D}{C}e^{-k_2a/2}}{e^{k_2a/2} + \frac{D}{C}e^{-k_2a/2}} \tag{3.21}$$

Comparing Equations (3.15), (3.16), and (3.17) we can write,

$$\frac{R_1}{R_2} = -\tanh\left(\frac{k_2 a}{2}\right) \Rightarrow \frac{D}{C} = 1 \Rightarrow D = C \tag{3.22}$$

And

$$\frac{R_1}{R_2} = -\coth\left(\frac{k_2 a}{2}\right) \Rightarrow \frac{D}{C} = -1 \Rightarrow D = -C \tag{3.23}$$

Therefore, in symmetric structures, the SPPs has two divisions: a symmetric (even H_x but odd E_z) and an anti-symmetric or asymmetric (odd H_x but even E_z).

There are two options for a symmetric structure: IMI (insulator-metal-insulator) and MIM(metal-insulator-metal).

Dispersion relation in a thin layer:

As can be seen in Fig 3.9, the odd modes possess frequencies ω_+, which are higher than the respective frequencies for single interface SPP, and the even modes lower frequencies ω_-. Odd modes have a fascinating property that the confinement of the coupled SPP to the metal

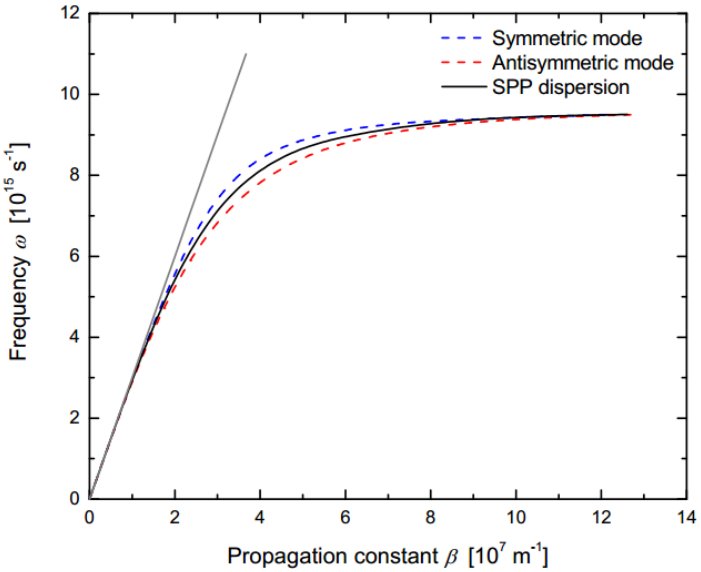

Fig. 3.9: The dispersion properties of both modes

film decreases with decreasing metal film thickness, as the mode changes into a plane wave. This phenomenon supports the homogeneous dielectric environment. Absorptive metals are defined with a complex ε(ω); this triggers a sharp increase in SPP propagation length. These are called Long-range surface Plasmon polariton (LRSPP). The even modes exhibit the exact opposite behavior as in that case, confinement to the metal increases as well as decreasing metal film thickness, ensuing reduction in propagation length. The following figure shows the dispersion properties of both modes of lossless Drude's metals. [29]

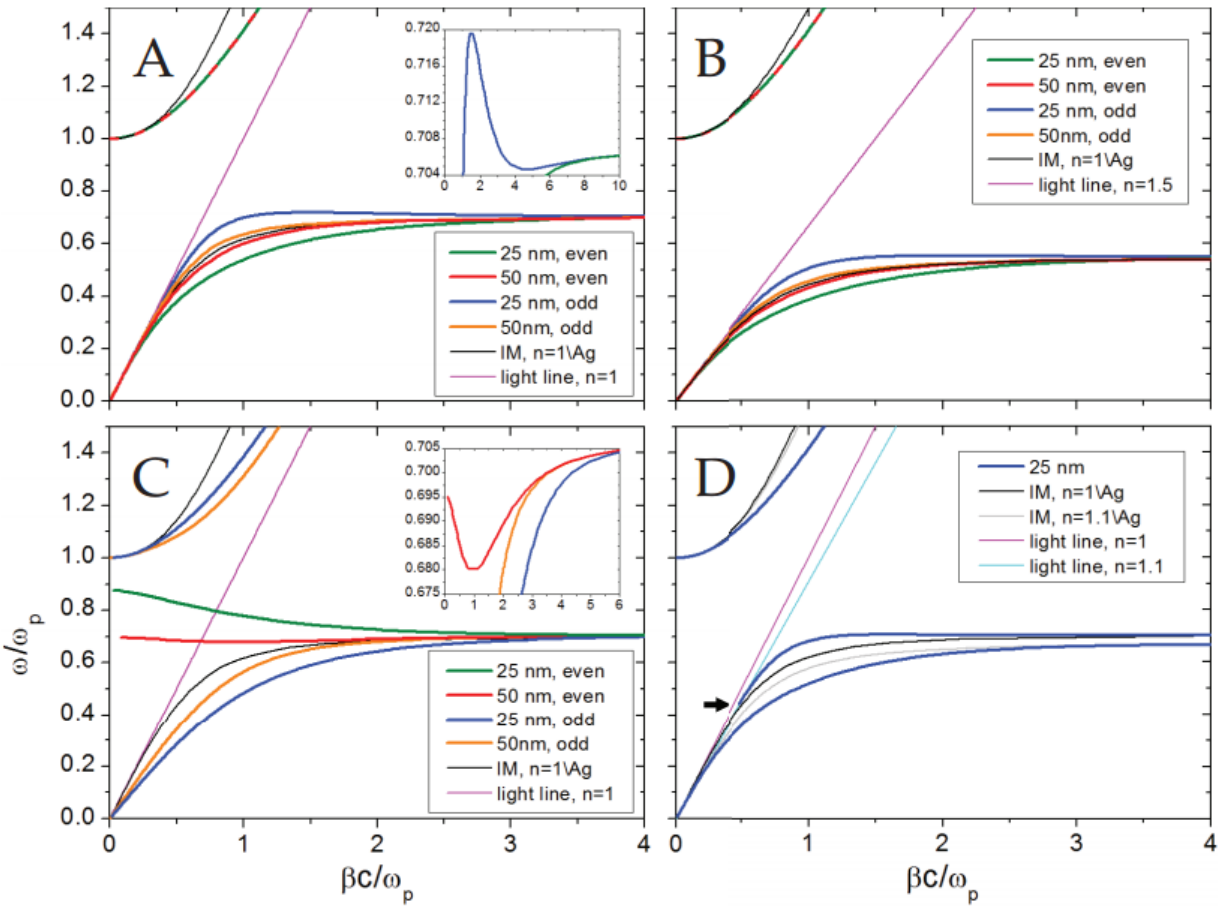

Fig 3.10: Dispersion profiles for different geometries and lossless Drude metals.

A) Symmetric IMI: 25nm and 50 nm metal layer immersed in free space.
B) Similar to the previous geometry, but the metal is immersed in a dielectric with n=1.5.
C) Symmetric MIM: 25 and 50 nm free-space layer immersed in metal.
D) Asymmetric IMI: 25 nm metal layer surrounded by free space and other dielectric with n=1.1.

3.6.2 Simulation by COMSOL Multiphysics

COMSOL Multiphysics is used to simulate the situation of an IMI structure. Here a silver layer of thickness 0.08 um is sandwiched between Silicon with dielectric constant 12.25. The dielectric constant of silver is taken from the result of Johnson and Christy [34]

As previous, the right and left boundary is set as Perfect Magnetic Conductor (PMC) while the upper and lower boundary (which are sufficiently far so that field decay to a very low value before reaching them) is set as Scattering boundary condition (SBC)

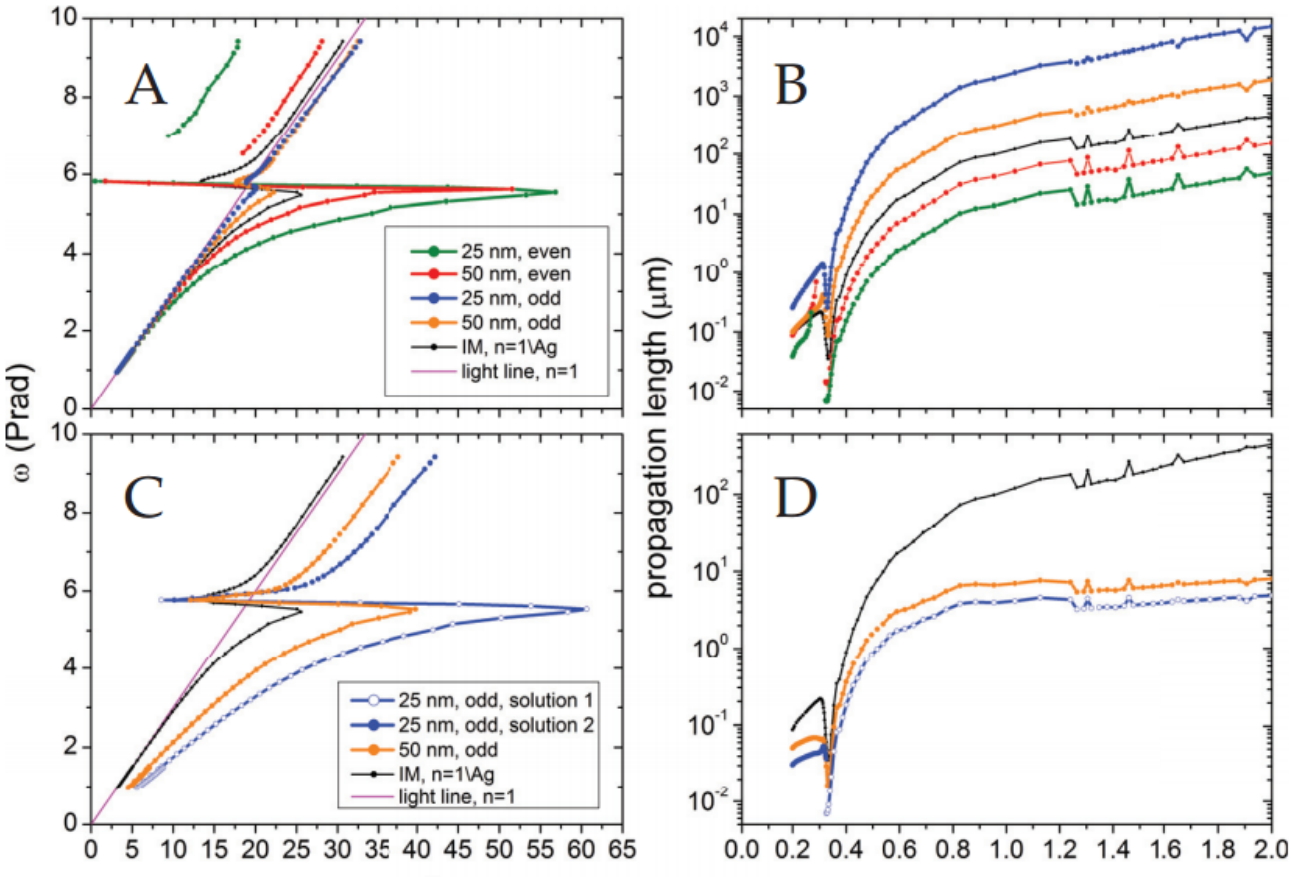

Fig. 3.11: Dispersion profiles, propagation lengths of symmetric geometries of metals

A, B) IMI: 25 and 50 nm silver layer wrapped up in the free space.

C, D) MIM: 25 and 50 nm free-space layer wrapped up in the metal (silver) .

Field profile

The surface plot of the three principal field components (E_z, H_x, E_y) for IMI structure is shown in Fig 3.12 and Fig. 3.13 for asymmetric and symmetric mode respectively.

Asymmetric mode:

The asymmetric mode has an odd H_x and E_y field profile but even E_z

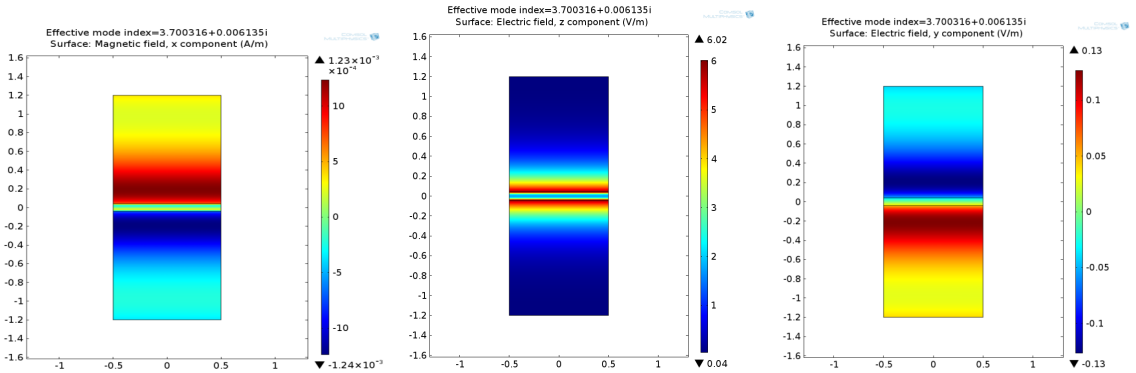

(a) (b) (c)

Fig. 3.12: Surface plot of the field profile for asymmetric mode in semi-infinite metal dielectric interface obtained by COMSOL. (a) H_x (b)E_z (c)E_y.

Symmetric mode:

The asymmetric mode has even H_x and E_y field profile but odd E_z

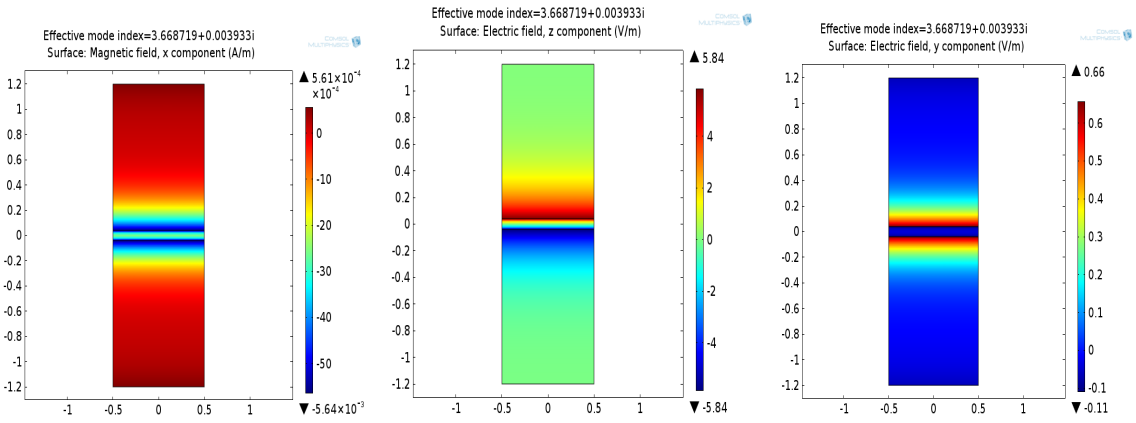

(a) (b) (c)

Fig. 3.13: Surface plot of the field profile for symmetric mode in semi infinite metal dielectric interface obtained by COMSOL. (a) H_x (b) E_z (c) E_y.

Dispersion Curves

The effect of core thickness is analyzed at wavelength 1.55 μm for which dielectric function of silver is obtained as -130.77 + 3.217i by interpolating data from Johnson and Christy [18].

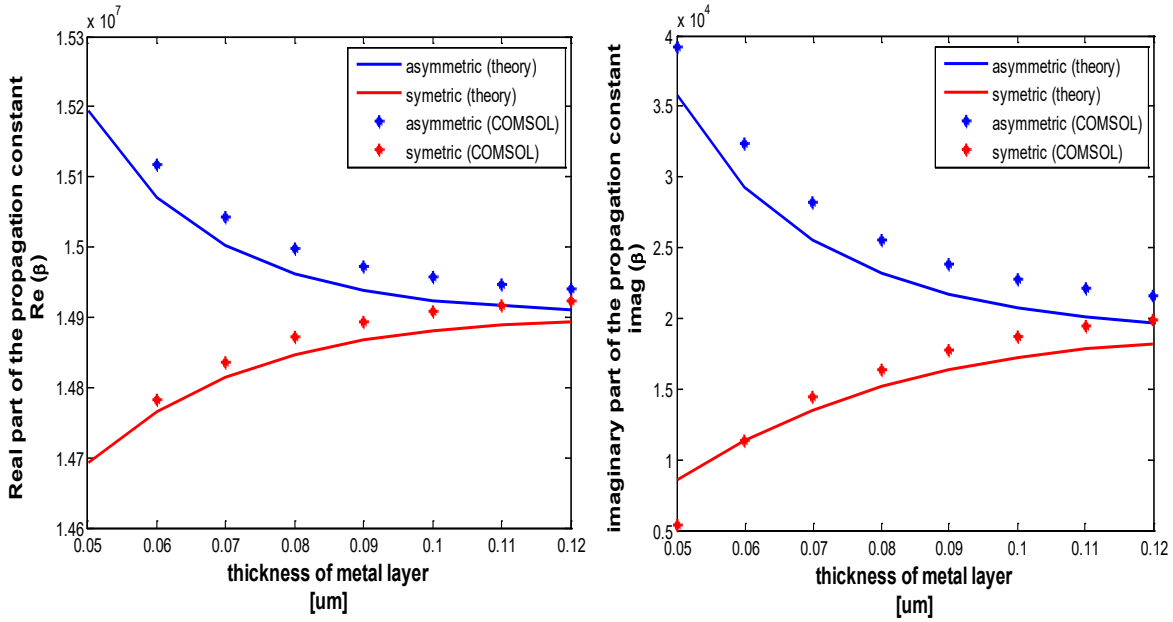

(a) real part (b) imaginary part

Fig. 3.14 Real and imaginary part of propagation constant for symmetric (red asterisk) and asymmetric (blue asterisk) mode of IMI structure obtained from COMSOL for different metal thickness. Theoretical values are shown in solid line. (For symmetric red line and for asymmetric blue line).

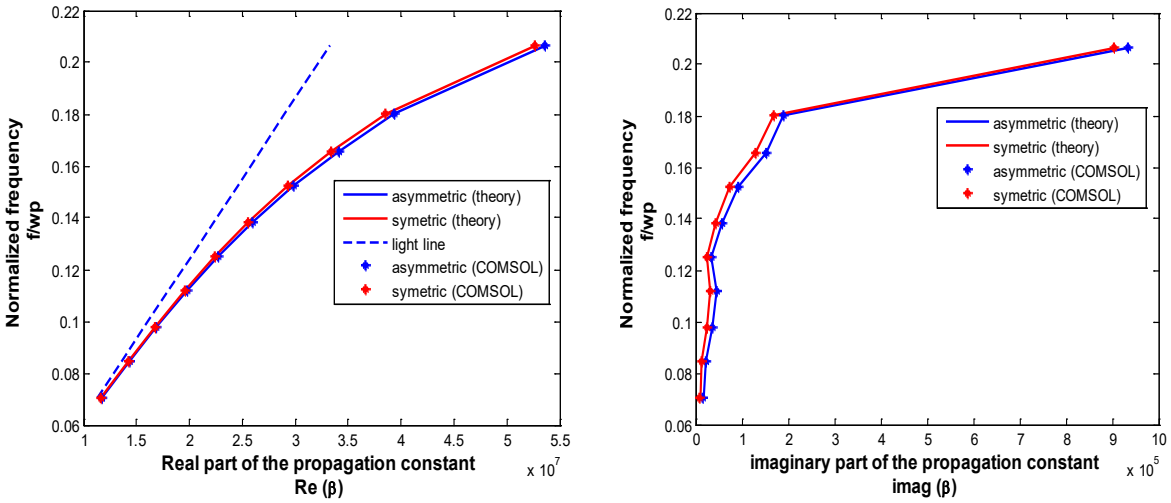

(a)real part (b)imaginary part

Fig. 3.15 Real and imaginary part of propagation constant for symmetric (red asterisk) and asymmetric (blue asterisk) mode of IMI structure obtained from COMSOL for different frequencies. Theoretical values are shown in solid line. (For symmetric red line and for asymmetric blue line).

The theoretical propagation constant value for symmetric and asymmetric mode are obtained by solving the characteristic equations numerically.

The effect of different wavelength is analyzed at core thickness of .08 μm with the dielectric function of silver obtained from Johnson and Christy [34]. Fig. 3.15 shows that as the frequency increases, the propagation constant also increases. Another observation found from the simulation is that at high frequencies, the higher effective index results in the field decaying very sharply. Whereas at a lower frequency, the effective index is lower and the field decays slowly. Fig. 3.16 and 3.17 clarify this observation.

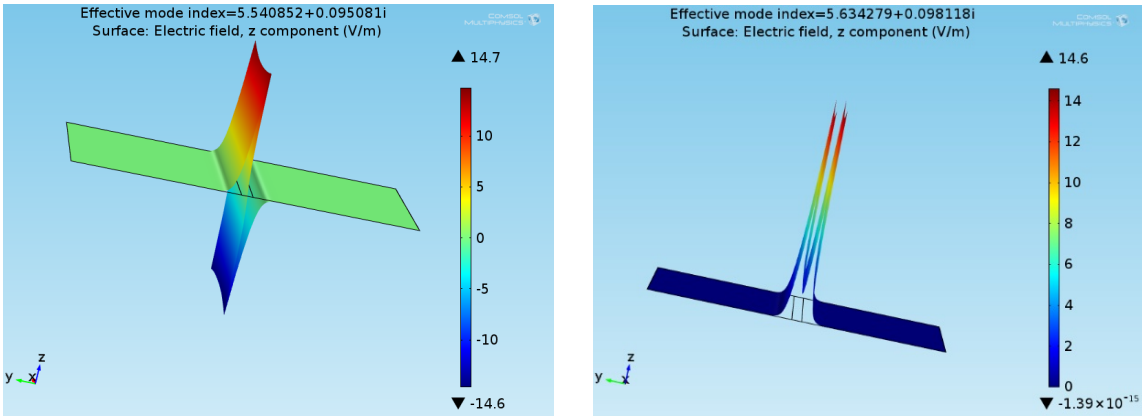

Fig 3.16: Height expression of electric field (at 1.88 eV).

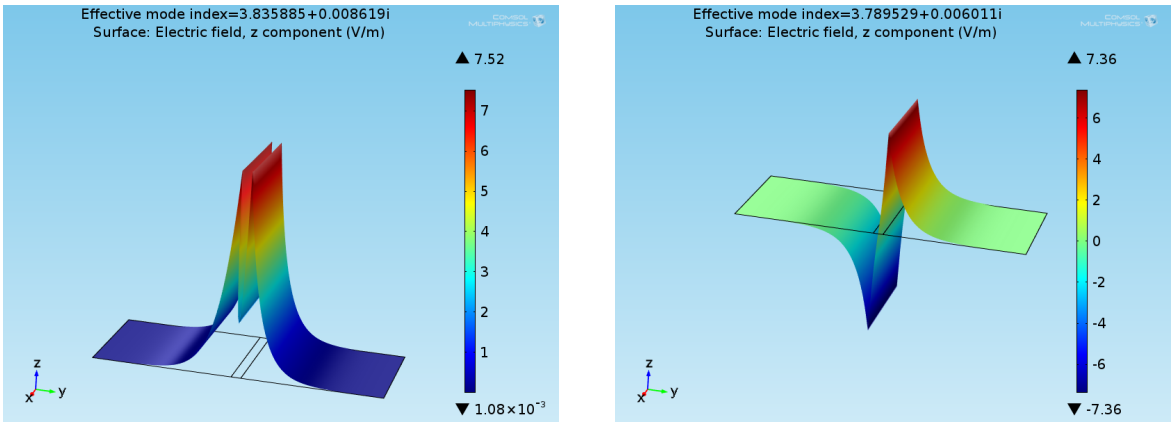

Fig 3.17: Height expression of electric field (at 1.02 eV)

3.7 Methodologies

1. The whole work considered three main types of plasmonic waveguides as follows:

   a) Metal strip waveguides

   b) Slot based waveguide

   c) Hybrid plasmonic waveguides with a metal cap and graphene layer.

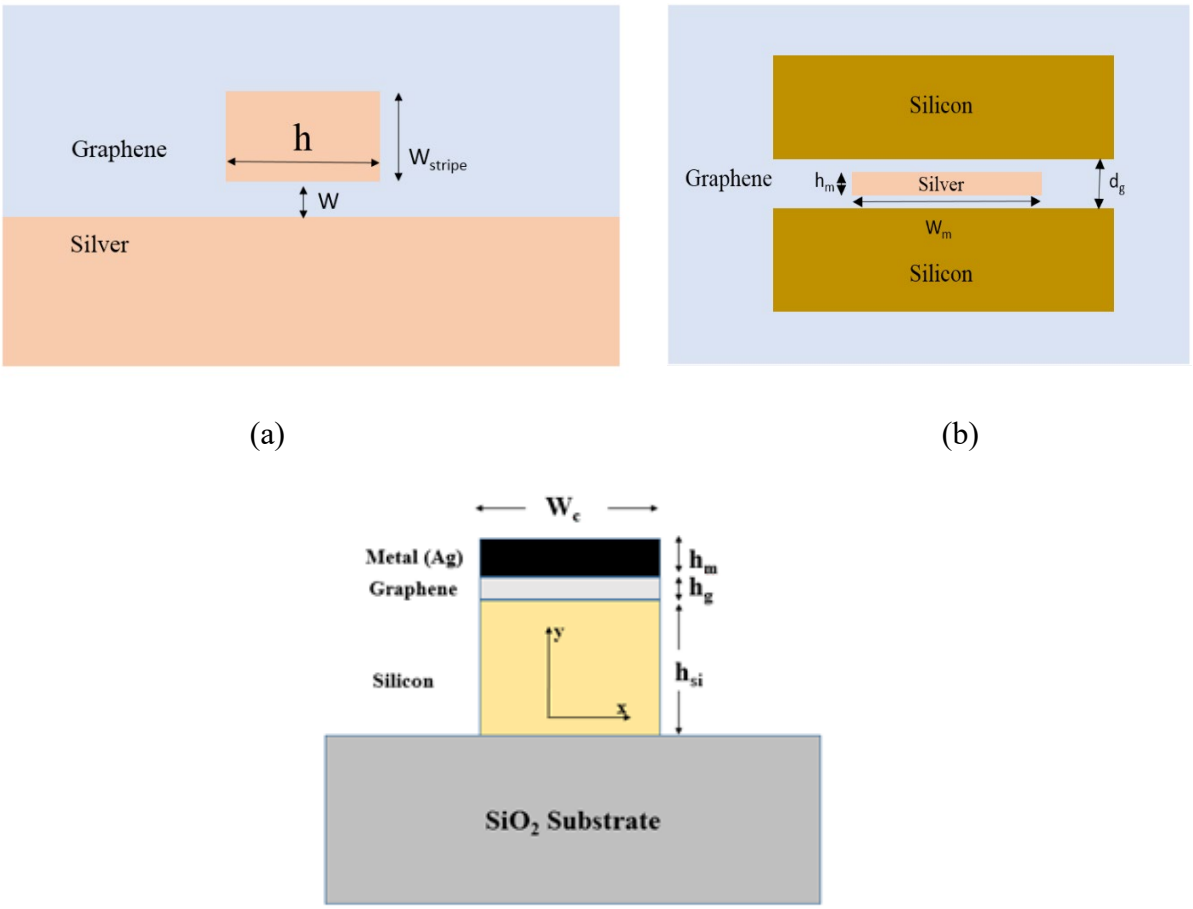

(a) (b)

(c)

Fig. 3.18: Cross section of the waveguides a) with metal strip and metal substrate and graphene in the gap, b) slot based waveguide and c) hybrid plasmonic with metal cap and graphene in the gap between metal and silicon rib

2. Fig. 3.18(a) demonstrates the structure of a metal strip waveguide where a graphene

layer is formed on a metal slab and a thin metal strip placed in graphene. 3.18(b) shows a slotted based waveguide embedded in graphene with a metal strip within.

3. The structure in Fig. 3.18(c) is the hybrid waveguide with a metal cap on top. A very thin graphene layer is present in between the metal and a high refractive index dielectric silicon (Si) rib. The silicon (Si) is placed on a silica (SiO_2) substrate.
4. The SPP modes should be found in ghaphene layer surrounded by the metal (Ag) and dielectric (Si) interface on opposite sides. This internal layer between metal and Si is used to guide the SPP wave through the lower indexed material graphene as the decay of SPP wave is reduced by it. Graphene has a unique characteristic of fine-tuning its refractive index by changing the Fermi level, and thus it acts as a suitable wave transmission material.
5. A full vectorial finite element method-based solver [45] is used to calculate the mode field and corresponding effective indices.
6. The FEM is incorporated with the terminal elements and the perfectly matched layers (PML) boundary to achieve more precise results [46]. The refractive indices are taken 1.445, 3.455 for SiO_2 and Si, respectively, as described in [9].
7. For metal Ag, we took the complex permittivity $\varepsilon_m = -129+i3.3$ at a wavelength of 1550 nm [47]. The complex permittivity, ε_g of graphene, is tuned as per description in [26] at the Fermi level, E_F =0.8 eV. The refractive index $n_g(\omega)$, though, is obtained by using the relation $n_g = \sqrt{\varepsilon_g}$ [1].
8. For the three models, the analysis of the propagation of surface plasmon polariton incorporates the calculation of effective mode area, propagation length, and the figure of merit using the method as described in the following sections. All these parameters will be compared between the different waveguides. We take Graphene as a lower indexed dielectric while the comparison was made with conventional SiO_2 from previous studies.

3.7.1 Effective mode area

The available measures of modal area are inherited from conventional waveguiding theory. Since the plasmonic waveguide can have sharp features that lead to rapid sub-wavelength level differences in the form of the model, these measures are somewhat inconsistent if we apply them for plasmonic mode. We need to find a definition that will consider the true extent of the plasmonic field distribution in order to consistently quantify the mode confinement. Out of many definitions found in the literature, we will provide three different definitions and compare them in our study of different waveguide structures.

The first definition A_1 depends on the peak energy density and defined as [48],

$$A_1 = \frac{1}{Max\{W(r)\}} \int_{A_\infty} W(r) dA \tag{3.24}$$

here, W(r) is the energy density,

$$W(r) = \frac{1}{2} Re\left\{\frac{d[\omega\epsilon(r)]}{d\omega}\right\} |\boldsymbol{E}(r)|^2 + \frac{1}{2}\mu_0 |\boldsymbol{H}(r)|^2 \tag{3.25}$$

A_1 is directly related to the non-linear properties like spontaneous emission rate enhancement or Purcell factor. Since A_1 depends on the maximum energy density, this measure may be misleading for a waveguide with very sharp features. This is useful to quantify the local field enhancement, which is not necessarily accompanied by strong confinement of total energy [48]. The second definition A_2 is a numerical measure needs amalgamation of energy density over the cross-section,

$$A_2 = \frac{\left[\int_{A_\infty} W(r) dA\right]^2}{\int_{A_\infty} W(r)^2 dA} \tag{3.26}$$

A_2 is usually a better measure since it takes into consideration of the overall field. This measure has a firm foundation in optical fiber theory [42]. However, it is potentially sensitive to energy distribution. The third definition A_3 is made, aiming to gauge confinement

irrespective of field distribution. A_3 is defined as the minimum area where exactly a portion η, of the mode's total energy, resides. Since η is a generic constant, A_3 is promised to be a shape-independent measure of confinement. We choose $\eta = 0{:}5$ in our study. So, it will be the minimum area where half of the mode's total energy will reside. In order to calculate A_3, we need to solve below minimization problem [48],

$$A_3 = min_{f(r)} \int_{A_\infty} f(r)dA \tag{3.27}$$

so that,

$$\int_{A_\infty} [f(r) - \eta]W(r)dA = 0 \tag{3.28}$$

We can iteratively solve the problem by using,

$$f(r) = 0, if\ \omega(r) < W_0, f(r) = 1, if\ \omega(r) > W_0 \tag{3.29}$$

where W_0 is the contour containing η (= 0:5) of the mode's total energy.

3.7.2 Propagation length

Although plasmonic structures provide extremely localized electromagnetic fields, there is an intrinsic cost involved in terms of the distance that the field can travel because of the damping inside the metal. If the plasmonic mode propagate harmonically in z-direction with field variation, exp [$i(\beta z - \omega t)$], the propagation distance is defined as the distance space that a mode can travel before the energy density decaying to $1{=}e$ of its original value [48],

$$L_p = \frac{1}{2Im\{\beta\}} \tag{3.26}$$

where, β is the propagation constant defined as $\beta = n_{eff}k_0$ and k_0 is the wave vector in vacuum equals to $\frac{2\pi}{\lambda_0}$. This definition is well established and consistent thorough out the literature.

3.7.3 Figure of merit

Another inconsistency arises when we try to evaluate the performance of a particular waveguide structure. Although most of the plasmonic waveguides works based on the same plasmonic phenomena, they exhibit different characteristics in terms of propagation, confinement and the trade-off between them. Figure of merit of a certain structure should take into consideration all these effects. Since the propagation distance is well defined, we need to choose a proper definition of confinement in order to quantify figure of merit objectively. We choose A_2, since this is quite consistent and provides almost similar behaviour of the geometry independent definition A_3. A_2 usually provides the highest value among the three definitions, so we will be using it mostly in order to avoid the probability of overestimation of confinement during the calculation of figure of merit and to avoid the complexity involved in calculating A_3. Nevertheless, as we argued, A_3 should be the most consistent definition of mode area. We will try to use all these definitions when we look for an effective mode area and compare whenever possible. Thus, the figure of merit is defined as a ratio between the normalized propagation length and normalized mode area [48],

$$FOM = \frac{L_p/\lambda_0}{A_2/A_0} \tag{3.27}$$

Here, $A_0 = \left(\frac{\lambda_0}{2}\right)^2$ is the diffraction-limited mode area and λ_0 is the vacuum wavelength.

3.8 Conclusion

The chapter ends by clearing up the ideas of the finite element methods and solid properties were combined to instigate actual models of Long-Range plasmon waveguides. Though almost every structure were built and analyzed in COMSOL, for the foremost part, the chapter explains all the related topic for modelling using basic finite element method simulator. Lastly, we discussed the equation for determining the key performance characteristics; propagation length, modal area and figure of merit.

Chapter 4

RESULTS AND DISCUSSION

4.1 Introduction

The analysis domain of the structure is divided into triangular edge elements to solve the Helmholtz equation and the effective refractive index $\left(\frac{\beta}{k_0}\right)$ and mode fields are obtained in the form of eigenvalue and eigenvectors, respectively. While all three types of waveguides have already been designed previously with conventional SiO_2 substrate, using graphene in this work has exhibited comparatively improved results in all aspects on an average. Furthermore, designing a hybrid waveguide with a metal cap and graphene has produced some exceptional results, as those will be demonstrated in this part of the report.

4.2 Metal Strip Waveguides

Metal strip on top of semi-infinitesimal metal slab structure is interesting because this is quite analogous to the microstrip waveguides, which are used at microwave frequency [79]. It is considered that one of the films having infinite height *h* (the metal slab) and another having finite length w_{strip} (the metal strip) placed at a finite gap w. According to [43], after studying the behavior for different gaps width and calculating different parameters as a function w_{strip} it is observed that propagation length decreases with decreasing w_{strip} since the fraction of power in the metal increases. Furthermore, it is interesting to notice that the propagation length of the strip actually goes beyond the slot at some length of w_{strip}. As w_{strip} increases, the modal area increases. This is because there is power in the dielectric gap region, and because of its lower index, confinement is not so high. But after some w_{strip} the edge mode begins to dominate. Although A_2 is no directly affected by the maximum power density, this will also affect the overall power distribution. So, after some value of w_{strip}, A_2 doesn't increase anymore. This behavior of the mode is also reflected in

propagation length [41].

In a similar study, it was observed that FOM of the strip increases with increasing w_{strip}, but it is always less than that of the slot waveguide. This FOM is also the indication of a comparison of the propagation length for a given mode area. So the performance of strip only approaches to that of plasmonic slot waveguide only when $w_{strip} \rightarrow \infty$.

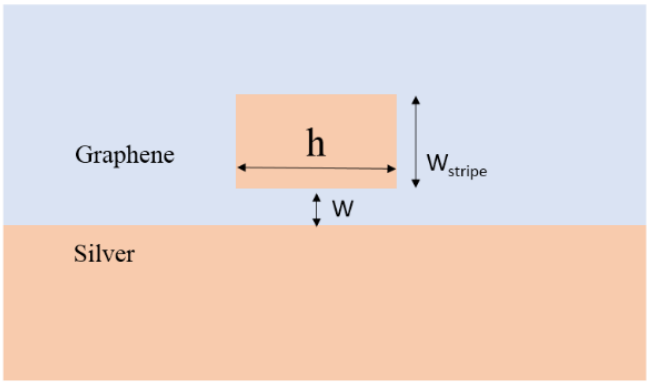

Fig. 4.1: Metal strip waveguide, Geometry of the waveguide which is made of silver (Ag) strip on top of the silver substrate and embedded in silica

The followings are the achieved results after analyzing a metal strip waveguide combined with a silver strip on top of the silver substrate based on silica. The Fig. 4.2 shows the optical power distribution P_z of the above-mentioned structure, where the fundamental mode for surface plasmon polariton has been found with $W_{strip} = 40$ nm, $h = 50$ nm, and $w_g = 10$ nm. The power distribution along x axis and y axis of the same structure has been shown in Fig. 4.3(a) and 4.3(b), respectively. It is visible that the surface plasmon effect was created along the surface of the metal strip, and confinement is maximum along x axis at the center of the graphene gap between stripe and metal substrate. Along y axis, the confinement is maximum at the interface of graphene and metal (Ag).

Fig. 4.4. exibits the variation of propagation length with the width of the metal strip, W_{strip}.

The gap between the strip and metal substrate has been varied as 10 and 20 nm and denoted as w_g. The discontinuous lines show the values of propagation length using SiO_2, whereas

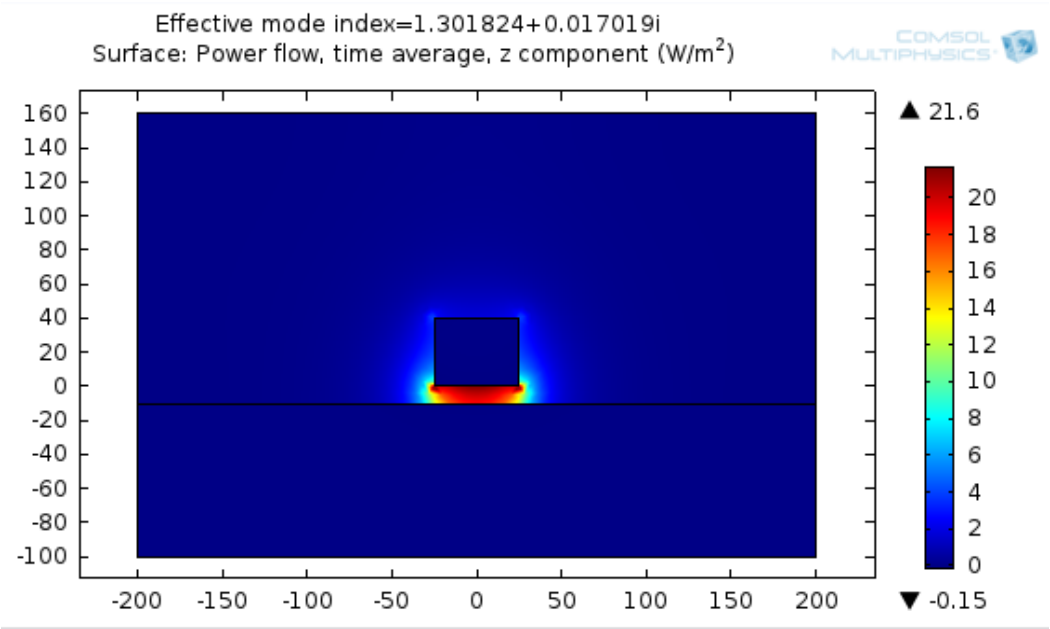

Fig. 4.2: Power distribution on the cross-section for fundamental mode

solid lines refer to values after using graphene. As per the study [13], the propagation length is shown as increasing as W_{strip} increases for SiO_2. It is further observed that propagation length increases from 4 µm to 6 µm as w_g rises from 10 to 20 nm. Now considering graphene in place of SiO_2, the propagation length increases to7 µm (for w_g = 10 nm) and 8 µm (w_g = 20nm).

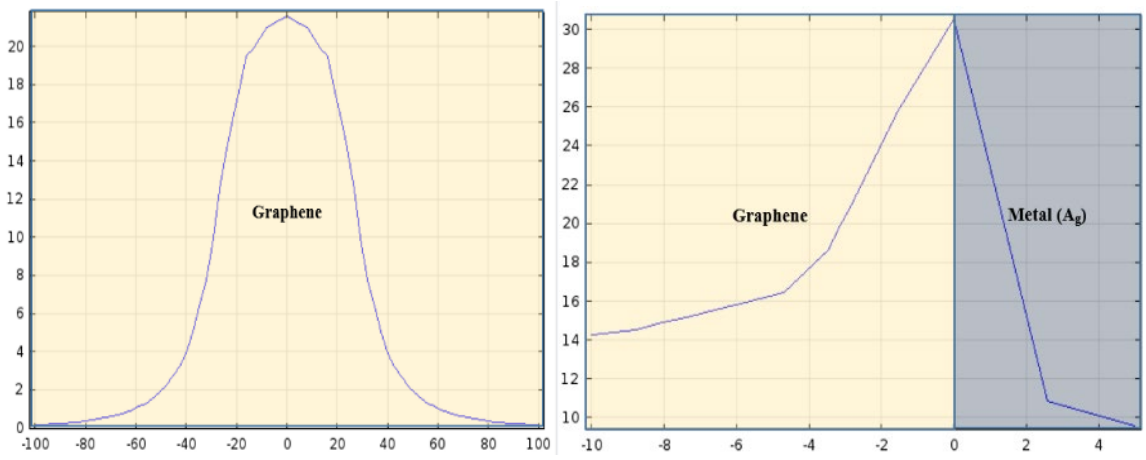

(a) (b)

Fig. 4.3 Variation of P_z for fundamental mode along x and y axis

Overall, although the improvement is not significant, graphene shows still a better result than that with SiO_2 (8.5 μm) with a gap of 20 nm between the strip and metal substrate in the graphene layer at the strip width of 40 nm at working wavelength of λ=1550 nm.

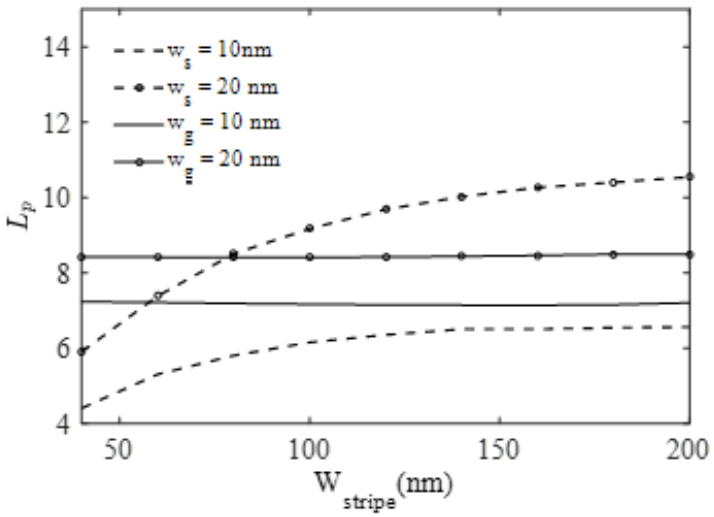

Fig. 4.4: Propagation length versus the width of metal strip

From Fig. 4.5, the normalized modal area has been demonstrated for both graphene and SiO_2 layers. While it is observed that for lower stripe width (40 nm) the modal area is almost similar for both graphene and SiO_2 (approximately 0.003 for W=10 and 0.008 for W=20), they both kept increasing by about 50%. We can also witness that for a static height of SiO_2 and

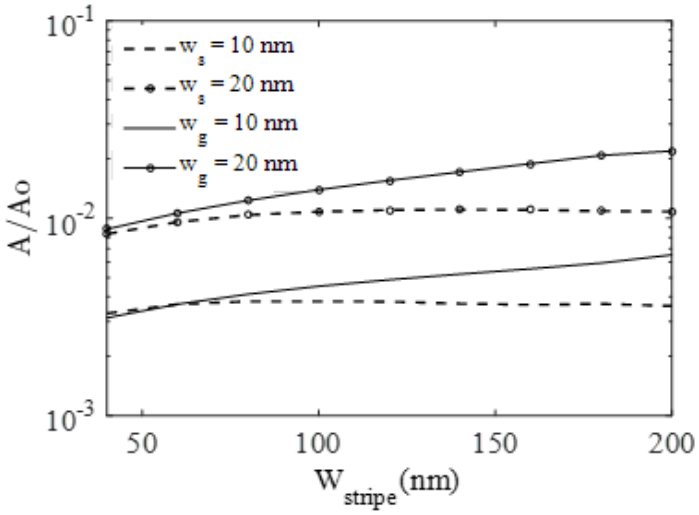

Fig. 4.5: Normalized modal area as functions of the width of metal strip.

graphene; the normalized mode area increases with the increase in W_{strip}. The increasing effective modal area with the increase of strip width and graphene or SiO_2 width refers weaker confinement of plasmonic wave propagation.

Fig. 4.6 shows the Figure of Merit (FOM) with the change of strip width (W_{strip}) and widths of gap in graphene (w_g) and in SiO_2 (w_s). FOM is the ratio of normalized propagation length and with modal area, and as an improved FOM refers to better result despite the value of propagation length and effective modal area, it is obvious from the result that using graphene instead of SiO_2 shows the FOM as maximum as 1500 at W_{strip} = 40nm compared to 800 nm for SiO_2. Additionally, between the gap witdh of 10nm and 20nm, the later gives better the result for both cases (graphene and SiO_2). For a metal strip it can be concluded that using graphene in the gap between the metal strip and metal substrate, the FOM was notably improved compared to SiO_2.

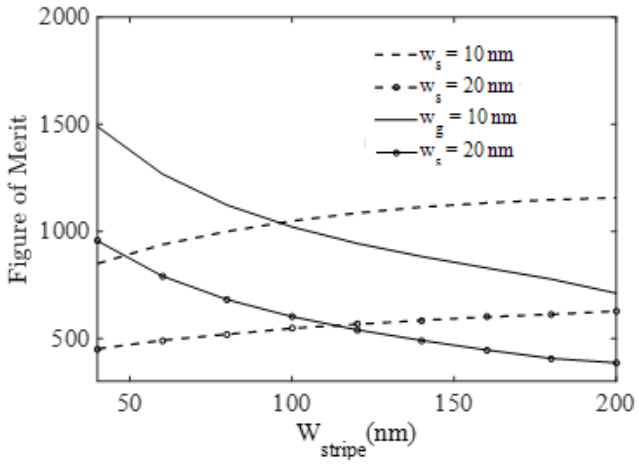

Fig. 4.6 Figure of Merit (FOM) as functions of the width of metal strip.

4.3 Slot Based Waveguides

This is another type of waveguide where two slots of Silicon are used on the base of graphene. In between the slots, a silver metal stripe is inserted where thickness of the strip is denoted by h_m and W_m indicates the width of the metal strip, whereas d_g is the thickness of the gap

between the slots. The low-permittivity region between them is denoted as the slot waveguide. The use of the two silicon bulks and their proximity help to produce a new long-range mode, which can be explained by the coupled mode theory [49,50*].

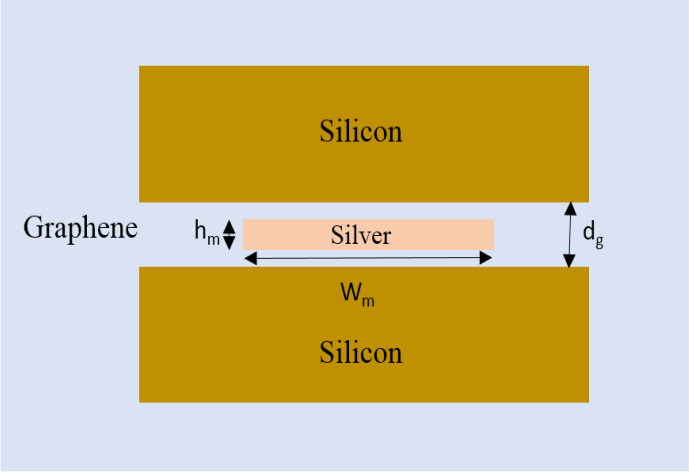

Fig. 4.7: Slot based waveguide, the geometry of a slot based waveguide with two slots of Silicon with metal inserted within them and embedded in grapheme

The above slot-based design has been analyzed, and optical power distribution, power variations along axes, propagation length, modal area, and figure of merits are discussed below. In Fig. 4.8, the optical power distribution P_z is shown, where the fundamental mode for surface plasmon polariton has been found with $W_c = 40$ nm, $h_m = 50$ nm, and $d_S = 70$ nm. The power distribution along x axis and y axis of the same structure has been shown in Fig. 4.9(a) and 4.9(b) respectively. It is clearly seen that surface plasmon wave propagates along the surface of the metal strip, and confinement is maximum at the center of the silica gap between stripe and metal substrate along x axis. Along y axis, the confinement is maximum at the interface of silica and metal (Ag).

Fig. 4.10 shows the propagation length versus width of the metal slot, W_c. The gap between the metal and metal substrate has been varied as 5 and 10 nm, which is reflected in d_s. The dashed lines show the values of propagation length using SiO_2, whereas solid lines refer to

values after using graphene. As per the study [49], the propagation length is shown as decreasing as W_c increases for SiO_2. W_c has been varied 40nm to 200 nm.

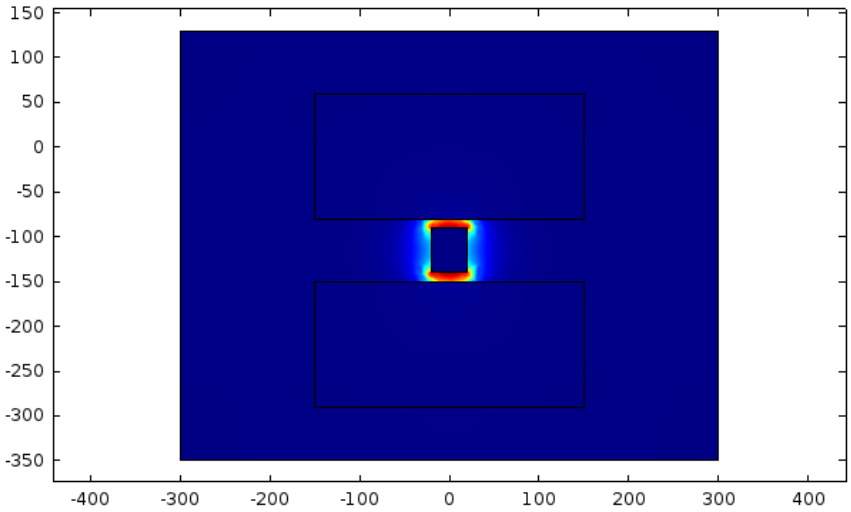

Fig. 4.8: Power density distribution on the cross section for fundamental mode

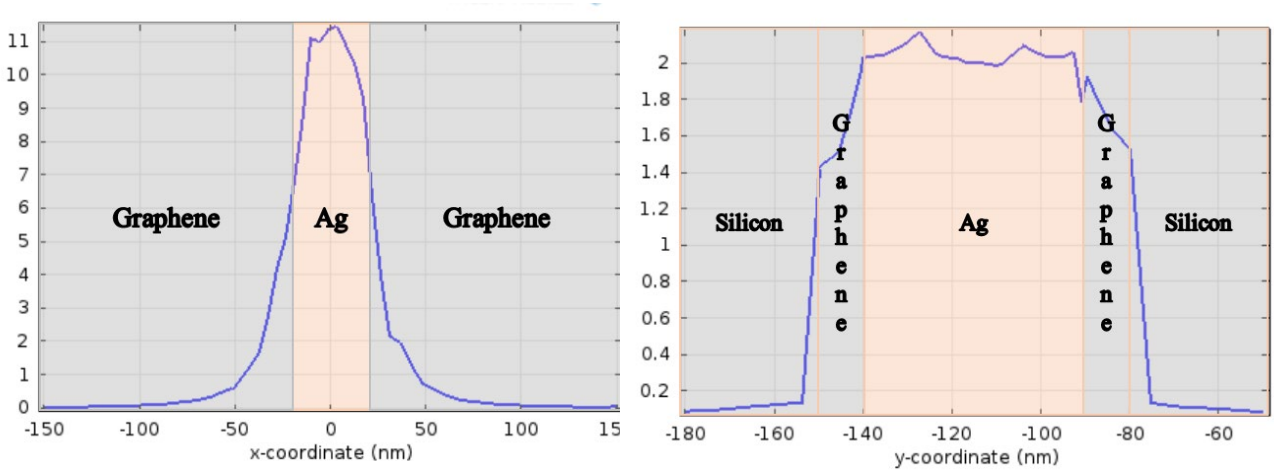

(a) (b)

Fig. 4.9: Variation of P_z for the fundamental mode along x and y axis

When h_m = 50nm and d_s = 70nm, we found the maximum propagation length of 224.8 nm, whereas, for d_s =60, it was 125.67 (Figure 4.10). As W_m increases, propagation length decreases in every case, and the same applies to FOM also. Modal area increases as W_m increases is an indication of weaker confinement, which is evident when h_m is 100nm (Fig. 4.11).

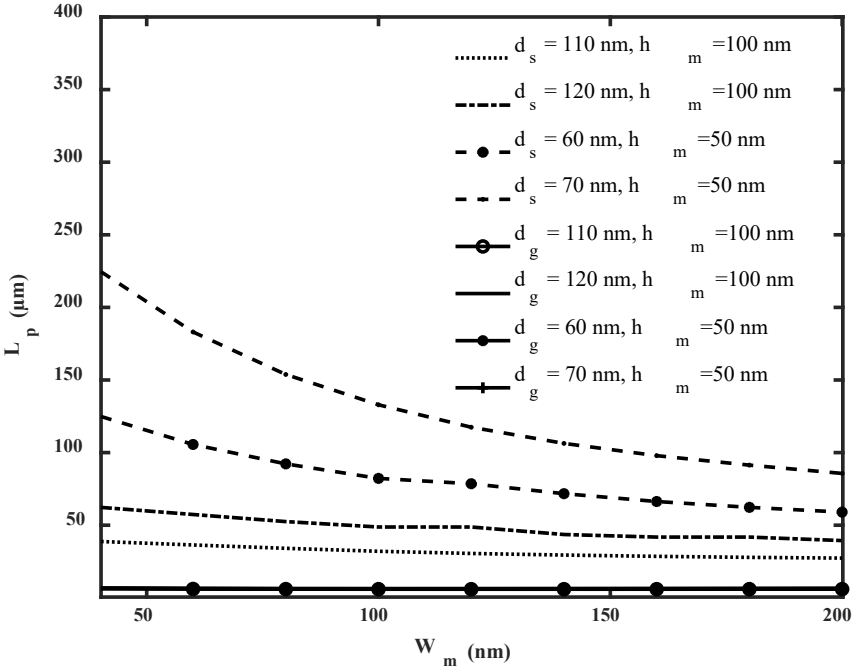

Fig. 4.10: Propagation length versus the width of metal (W_m).

We clearly see that the highest figure of merit is achieved only when d_s=60nm and h_m=50nm at the metal width, W_m, of 40nm and that is 4915 (Figure 4.12). However, in this case, the propagation length and modal area are 125nm and 0.0182 respectively.

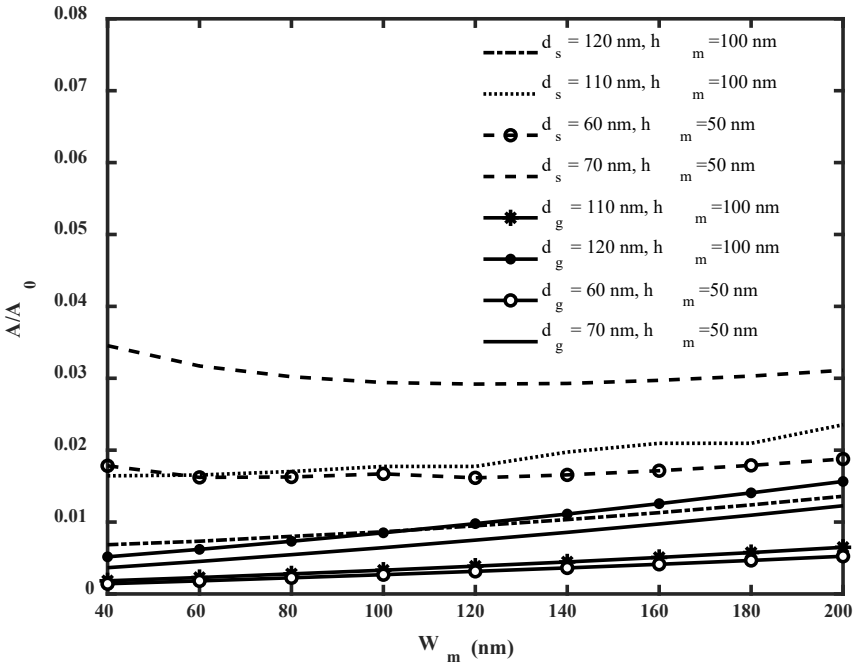

Fig. 4.11 Normalized modal area versus the width of metal strip.

Overall, For h_m = 100nm, no significant changes have been observed in Figure 4.8, 4.9 and 4.10, compared to those for h_m =50 nm. It also observed that for this design the graphene did exhibit any significant results. The propagation length, in this case, was steady at around 6nm regardless the changes in W_m. Additionally, the highest figure of merit was as much as 2920 nm at the metal width of 40nm. It, therefore, can be mentioned that silicon rather showed better result here compared to graphene.

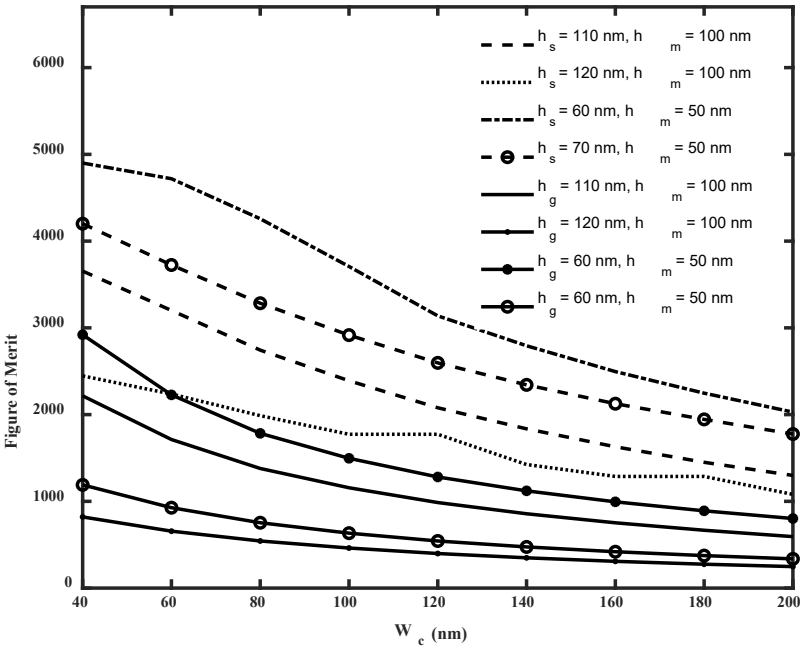

Fig. 4.12 Figure of Merit (FOM) as a function of width of metal strip.

4.4 Hybrid Plasmonic Waveguides

The typical waveguides, as discussed above, are composed of one metal and one dielectric. Confinement much smaller than the diffraction limit of light has been achieved in these structures with moderate propagation length at the range of few tens of micrometers. But for practical application e.g. photonic integration, this length is not sufficient. It has been reported in several papers hybrid plasmonic waveguides consisting of three material systems (metal-low index dielectric-high index dielectric) can provide better performance than the

conventional pure plasmonic waveguides [44]. These type of waveguides utilize the coupling between the SPP and the conventional dielectric mode.

4.4.1 Hybrid plasmonic waveguide with a metal cap

Another interesting hybrid structure is the metal cap on top of a Si rib separated by thin silica film, as shown in Figure 4.13 [43]. Even a simplified structure is possible with the rib replaced by a slab which is even easier to fabricate. It is evident from this study [yassin] that power is well confined in the low index silica region. When we increase the width *w* of the waveguide, there will be more power in the Si rib, so the propagation length increases with the width [44]. Also, after reducing the silica film thickness h, the fraction of power in the metal increases, so the thicker the silica film, the longer the propagation length is. It is noticed that for a thin film, the propagation distance does not vary a lot along with the width. But for large film thickness, there is huge variation when the width is increased. For small h, more power in the metal, the mode in the Si rib and the surface plasmon mode are more strongly coupled and hence, the effective mode area is very small.

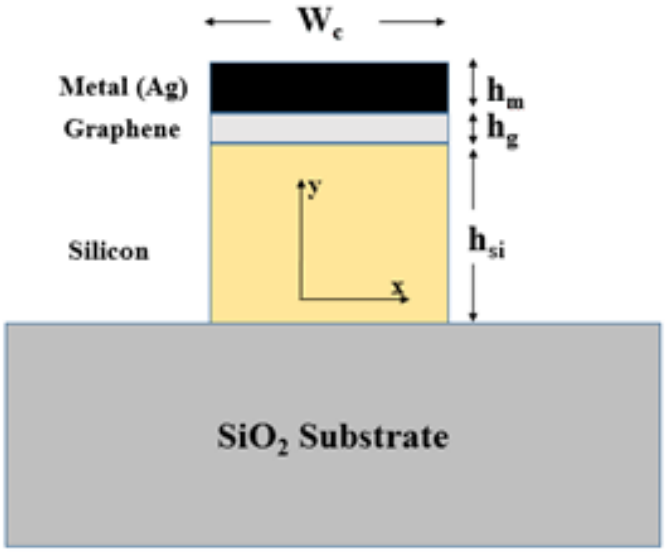

Fig. 4.13 Cross-sectional geometry of the hybrid metal cap with rib structure (left), when rib replaced with slab (right)

Because of this strong coupling with the surface plasmon mode, the propagation distance cannot increase a lot along with the width. Surface plasmon mode does not really depend on the width of the waveguide.

In the following part, the designed hybrid waveguide with metal cap has been analyzed

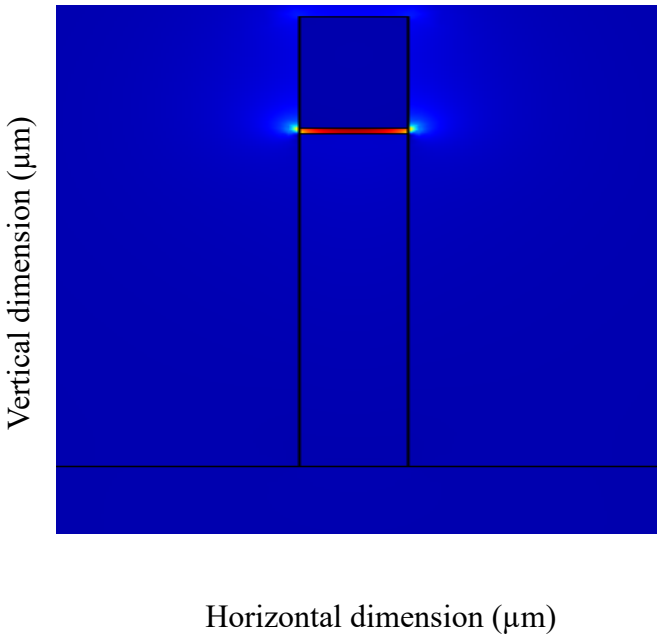

Fig. 4.14 Power density distribution on the cross-section for the fundamental mode

and power distribution, propagation length, modal area and figure of merits are observed. For the design, the distribution of the optical power P_z is shown in Fig.4.14 where the fundamental mode for surface plasmon polariton has been found with W_c = 50 nm, hg = 5 nm, and h_{si} = 300 nm. The figure clearly depicts the nanoscale energy confinement. Fig. 4.15 (a) and (b) show the power distribution, P_z along the x and y axis for the same structural dimension. It is clearly seen that surface plasmon wave propagates along the surface of the metal and the confinement is highest at the center of the metal cap along the x axis. Along the y axis the fundamental mode confinement occurs at graphene layer as the power P_z distribution is almost zero in Si or Ag layers.

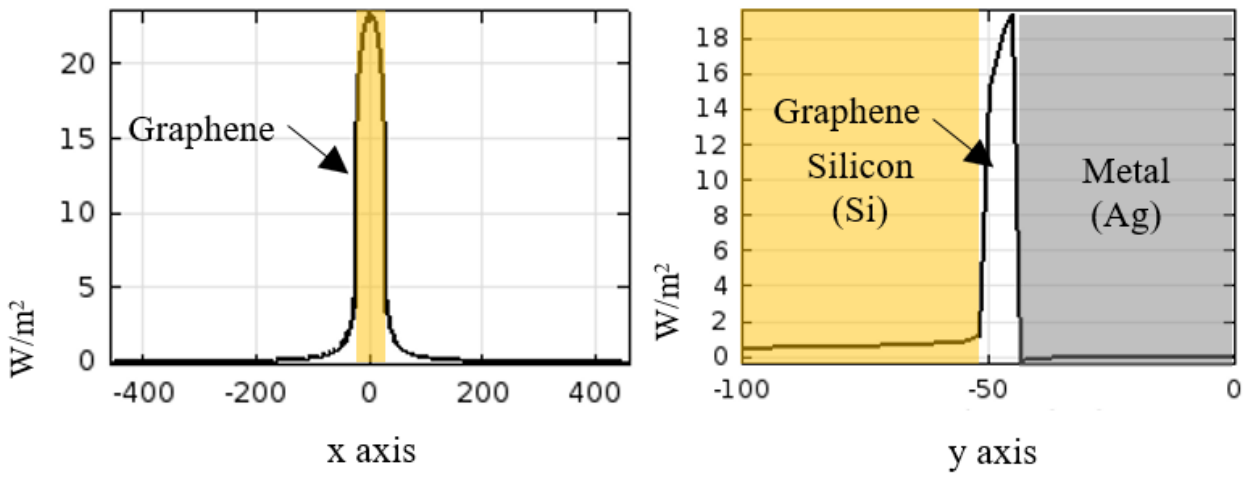

(a) (b)

Fig. 4.15: Variation of power (P_z) for the fundamental mode

As this specific structure with graphene demonstrates surface plasmon propagation, thus can be investigated further. Fig. 4.16 shows the propagation length versus metal cap width, W_c. In this case, the height of the silicon rib, h_{si} is taken 300 nm and the height of the metal cap, h_m is kept 100 nm. The layer of graphene, h_g is varied as 5 nm and 50 nm. According to a study [13] while SiO_2 layer is used between silver and silcon rib, the propagation length increases with the increase in W_c. The propagation distance becomes 401 µm from 76 µm when the core width increases from 50 nm to .45 µm while taking the height of SiO_2 layer, h=50 nm. The propagation length decreases further with a thinner layer of SiO_2, h= 5 nm, and from the sketch, we can pick the maximum value of propagation length 67 µm with a metal cap width of 0.45 µm. On the other hand, the highest value of propagation length is achieved 1814 µm (~1000 x λ) while we use graphene layer of height, h_g = 5 nm and width of metal cap, W_c = 50 nm at working wavelength of λ=1550 nm.

From the graph, it is clearly seen that for the graphene layer, the propagation length of the plasmonic wave decreases while the width of the metal cap, Wc, increases, and the trend is exactly reverse as reported in [13]. The propagation length decreases from 103 to 102 µm scale while we tune the graphene layer height, hg from 5 nm to 50 nm. It should be noted

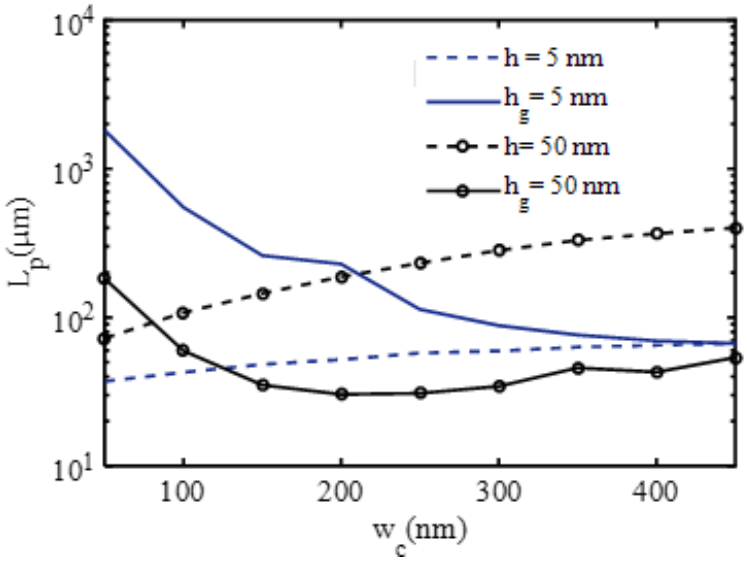

Fig. 4.16: Propagation length versus core width.

that the working equation of propagation length in the ref. [13] is different, and according to the equation of propagation length used in our investigation, the value of propagation length in the study [13] should be half of the value, which is shown in the Fig. 4.16. Thus, the overall propagation length is enhanced to a great extent while we use the graphene layer instead of silica in between silver and silicon.

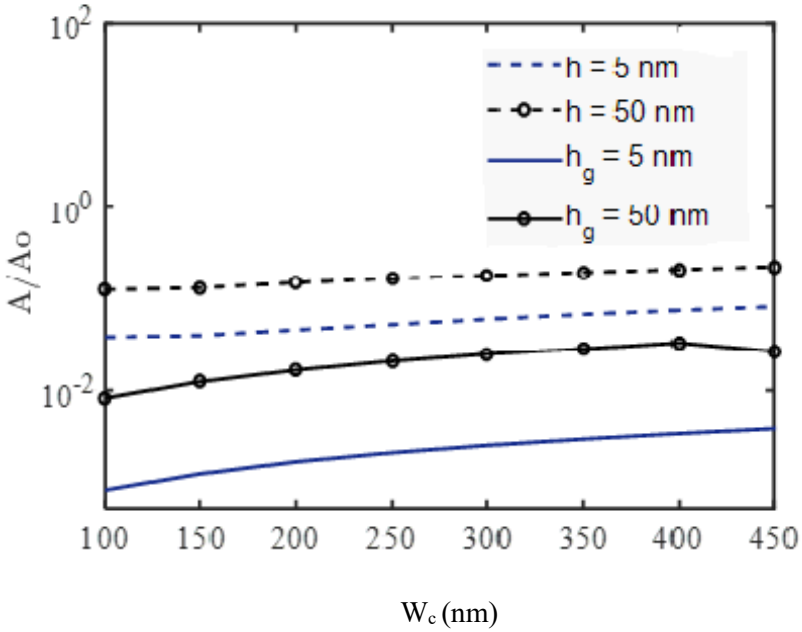

Fig. 4.17: Normalized modal area versus core width.

Fig. 4.17 exibits the values of normalized modal area while the width of metal cap, W_c is varried. In this case, the height of the silicon rib, h_{si} and the height of the metal cap, h_m are kept 300 nm and 100 nm, respectively. Dashed lines show the values of propagation length using SiO_2 layer in between silver and silicon [13]. The height of silica layer, h decreases from 50 nm. of 10^{-1}. We can also observe that for a fixed height of silica, normalized modal area increases with the increase in W_c. Higher W_c and h result larger surface area as well as larger effective modal area for plasmonic wave propagation, which offers a very weak confinement of photons.

When we use graphene layer instead of silica, the normalized modal area decreases to a much smaller range of 10^{-3} with a height of graphene layer, h_g = 5 nm. If we take the height h_g = 50 nm, the normalized modal area increases, and it further increases with increase in W_c. The figure shows the increasing trend of the normalized modal area with larger W_c still, the values are smaller with graphene than that of silica.

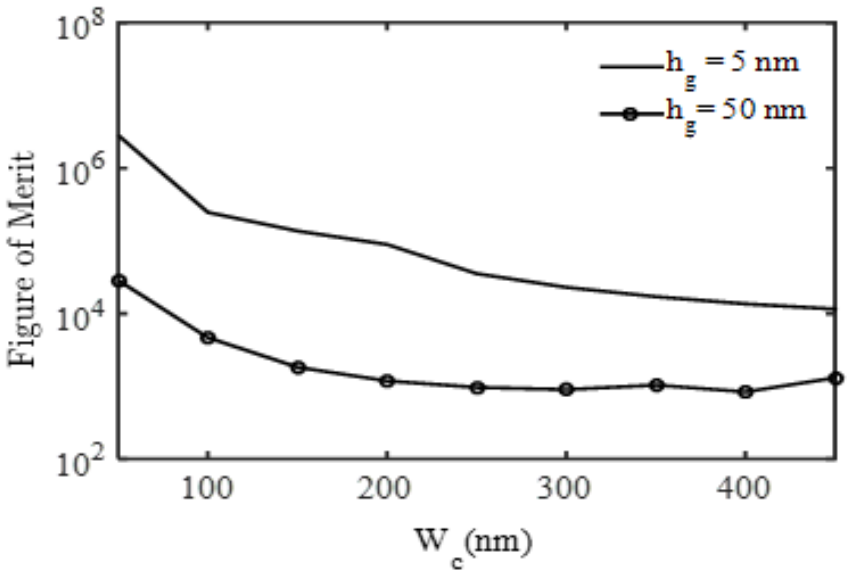

Fig. 4.18: Figure of Merit (FOM) versus core width

Fig. 4.18 shows the Figure of Merit (FOM) with the change of width of the metal cap, W_c for the hybrid waveguide structure using graphene with h_{Si} = 300 nm and h_m = 100 nm. For

nanoscale fabrication, it is a challenge to keep the device very small with a long propagation length and tight confinement. When using SiO_2 layer for the hybrid waveguide shown in Fig. 4.18 instead of graphene, the higher width of the metal cap, the propagation length becomes larger and results in a higher effective modal area. As the FOM is the ratio of normalized propagation length with the modal area, in spite of having higher propagation length, overall FOM decreases with a larger width of the metal core, W_c. Thus a trade-off between propagation length and the effective modal area is required, and the geometrical tunability for enhancing the propagation characteristics is limited. While we use graphene, the propagation length decreases with increasing W_c, also the trend is similar for the normalized modal area. The highest figure of merit reaches the numerical value above 106, which can be achieved with the geometry of hg = 5 nm and W_c = 50 nm. The overall surface area covered by plasmonic propagation is 5x50 $nm^{2,}$ which qualifies the range of nanoscale fabrication.

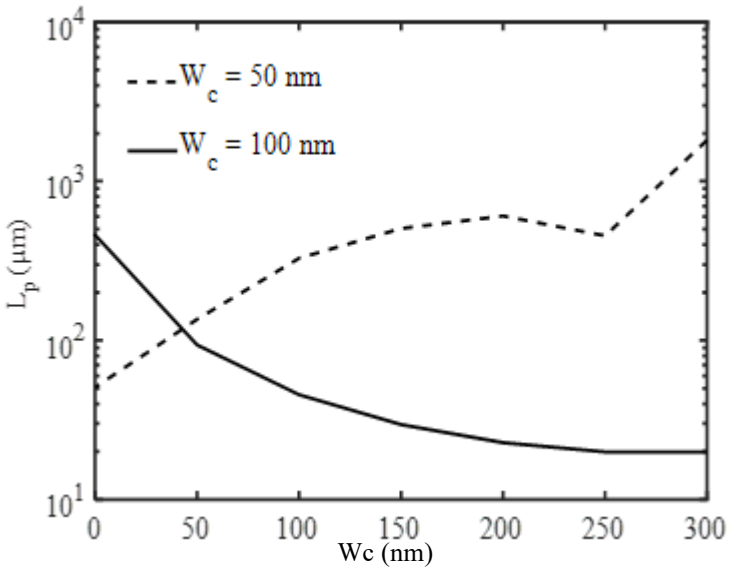

Fig. 4.19: Propagation length (L_p) versus Si rib height.

The unique transmission properties of graphene aid in guiding the SPP wave through the structure. The fundamental mode confinement of SPP wave is possible within the surface area of only 250 nm^2, thus the modal area is significantly low in this case. The waveguide consisting of a graphene layer requires rather less optimization than other models (with

silica), as it shows higher propagation characterstics in the lower scale of geometry. So there is flexibility of choosing the dimension in designing long range surface plasmon waveguide, which is a very promising. Fig. 4.19 shows the the trend of propagation length with the change in Si rib height, h_{si} taking the height of graphene layer , h_g = 5 nm and metal cap height, h_m = 100 nm. We only examined the propagation length keeping above dimension fixed (h_g = 5 nm and h_m = 100nm) because the effective modal area is minimum for this geometry. The main intention is to observe the change in propagation characteristics. The dashed line shows the change in propagation length, taking the width of the rib, W_c = 50 nm when the height of Si rib is varied towards zero. For zero height of Si rib, the structure becomes like a slab waveguide. When W_c = 50 nm, the propagation length decreases below 100 μm and when h_{Si} is smaller than 50 nm. The result is rather satisfactory while taking W_c = 100 nm, although the maximum propagation length is not achieved. When h_{Si} is smaller, the propagation length becomes larger, and at h_{Si} = 0 nm, we got the propagation length 450 μm, which is also promising.

4.5 Result

For W=10 nm (metal strip)

W_{sripe}	A/A_0 (SiO_2)	A/A_0 (Graphene)	FOM (SiO_2)	FOM (Graphene)	Lp(SiO_2)	Lp (Graphene)
40	3.30E-03	0.002542848	850	1132.591089	4.4	4.464011
60	3.67E-03	0.002721606	939	1256.139585	5.3	5.299011
80	3.79E-03	0.002818112	1000	1326.780263	5.8	5.795474
100	3.79E-03	0.00286419	1049	1366.562849	6.15	6.066848
120	3.78E-03	0.002882962	1086	1386.093957	6.35	6.193888
140	3.69E-03	0.002889299	1113.85	1378.140283	6.5	6.171883
160	3.65E-03	0.002894365	1133	1423.965564	6.5	6.388289
180	3.69E-03	0.002932818	1148	1407.190823	6.54	6.396903
200	3.60E-03	0.003179771	1157	1305.962563	6.56	6.436627

For W=5 nm (metal strip)

W_{sripe}	A/A_0 (SiO_2)	A/A_0 (Graphene)	FOM (SiO_2)	FOM (Graphene)	Lp(SiO_2)	Lp (Graphene)
40	0.00833	0.008808	452	956.1438	5.9	8.421465
60	0.00958	0.010627	492	791.7046	7.38	8.413664
80	0.0104	0.012328	520	681.8773	8.5	8.405917
100	0.0108	0.013955	548	602.4466	9.17	8.406967
120	0.01102	0.015551	567	541.2347	9.68	8.41701
140	0.01106	0.017175	585	491.0964	10.02	8.434513
160	0.01103	0.018914	601	447.2049	10.26	8.458484
180	0.0109	0.020826	613	407.5928	10.4	8.48852
200	0.01081	0.021933	628	387.0918	10.54	8.489927

For h_g =50 nm (Hybrid waveguide with metal Cap)

W_c	A/A_0 (SiO_2)	A/A_0 (Graphene)	FOM(SiO_2)	FOM (Graphene)	Lp(SiO_2)	Lp (Graphene)
50	0.004128	0.004103		28643.97		182.1493
100	0.123927	0.008238	280.6314	4671.04	53.9056	59.64593
150	0.129828	0.012374	357.4521	1830.98	71.9313	35.11826
200	0.148069	0.016504	408.7881	1186.69	93.8197	30.3568
250	0.1647	0.020604	456.6152	967.39	116.567	30.89416
300	0.179721	0.024619	500.1049	902.44	139.313	34.4369
350	0.19367	0.028398	535.5735	1040.88	160.773	45.81681
400	0.208155	0.03294	558.1635	840.05	180.086	42.88987
450	0.223176	0.026517	565.2417	1307.57	195.53	53.74314

For h_g nm (Hybrid waveguide with metal Cap)

W_c	A/A_0 (SiO_2)	A/A_0 (Graphene)	FOM(SiO_2)	FOM (Graphene)	Lp(SiO_2)	Lp (Graphene)
50		0.000416		2817929.1		1814.933
100	0.03809	0.000828	375.0022	86360.50	22.14	110.878
150	0.0397	0.001231	401.7266	136691.14	24.72	260.8673
200	0.045601	0.001657	374.0419	89035.25	26.4378	228.6535
250	0.052039	0.002065	354.3734	35380.34	28.5837	113.2688
300	0.059549	0.002474	323.6283	22997.97	29.8712	88.20424
350	0.06706	0.002886	299.7681	17041.73	31.1588	76.23814
400	0.074034	0.003304	279.0104	13593.57	32.0172	69.6209
450	0.081009	0.003731	258.4067	11537.82	32.4464	66.71989

Chapter 5

CONCLUSIONS

5.1 Conclusion

In this work, a metal strip, a slot based waveguide, and a hybrid plasmonic waveguide with a metal cap have been used, and they were examined with the conventional SiO_2 and novel material, graphene. For some nanoscale fabrications and subwavelength applicabilities, the overall size of the structure, propagation length, effective modal area, confinement of the wave, and Figure of Merit (FOM) are fundamental features as considered by the researchers. This work has emphasized on the material rather than the design of the waveguides and is successful in demonstrating that by using graphene, more miniature design is possible as per the present and upcoming future applications.

While analyzing metal strip waveguides, it was found that, despite a slight improvement in propagation length and effective modal area, the Figure of Merit (FOM) was significantly improved (approximately by 50%) compared to conventional SiO_2 after using graphene, and the better result was found with narrower gap width between the strip and the metal substrate. Besides, the propagation length was observed as much as 8.5 μm, which is about 75% higher than that of SiO_2. The lower gap width of 10 nm exhibited a better result.

On the other hand, the slot based waveguide demonstrated an improved result for SiO_2 rather than graphene, where the performance remained almost constant with the change in metal width. It also can be commented that the lower the metal width is, the better the result overall. The maximum propagation length was found as 224 nm when the silver height of silver was 50 nm, and with the gap d_s of 70 nm at a metal width of 40 nm, whereas, figure of merit was maximized to 4951 by setting d_s as 60nm.

In the following portion of the work, graphene layer-based hybrid plasmonic waveguide has been examined. The highest propagation length achieved here is 1814 μm with a very trivial confinement area of about 250 nm^2. The propagation length gets higher when the width of the metal cap reduces, and the trend matches for both graphene layers of 5 and 50 nm. As the smaller metal cap width contributes to the reduced plasmonic wave propagation surface area; thus, the normalized modal area also decreases with a thinner layer of the metal cap. The overall performance indicator, the figure of merit, elevates in the range of 10^6 when we keep graphene layer 5 nm, which is much better than that of the silica layer, surrounded by metal and silicon.

After comparing and analyzing both metal strip and hybrid plasmonic waveguides with a metal cap in terms of conventional SiO_2 and graphene, clearly, graphene exhibited superior results at a lower level of width, and that refers that designing plasmonic waveguides with graphene could be a better candidate for nanoscale fabrication and subwavelength operability. The unique properties of this plasmonic structure with graphene demonstrate improved propagation profile, which can open a new direction to design nanoscale photonic devices.

5.2 Future scopes of the work

Photonic components attract a lot of attention because of fast, robust response to electromagnetic interference and higher energy efficiency. Further works could be done to expedite the use of hybrid plasmonic waveguides in linear and nonlinear applications. The drawbacks of traditional photonic devices, such as limited by diffraction, traditional operations, and dominated by ohmic losses, can be evaded by introducing a “hybrid” device that uses metals merely to confine the light.

The main weaknesses of long-range – SPP stripe waveguides are the dependency of high polarization and huge ohomic loss. The main challenge is getting the higher propagation keeping the tight confinement. Ongoing researchers currently focus on placing the waveguide in advance medium and pulsating it with a laser to reduce the propagation loss. This device has a lot more applications in designing high-efficiency lasers.

Studies can be carried on a plasmonic diming device, housed by a metal nanorod and a glass layer used to coat the outer surface, an upconverting nanoparticle. In this manner, the upconverting nanoparticle (UPN) is placed in between a nanorod and a nanoparticle to make a sandwich model. Thus, the nanoparticle can be quenched by the metal nanosphere. When one of the links is broken by the interaction of a specific molecule of interest, the upconverting nanoparticle will glow. This can be used as a background-free biosensing method that will contribute greatly to diagnose the illness of the human cell and can be used to cure complicated diseases like cancer. We also can attach the nanoparticles with metal nanorods to create the boosted luminescence. This can be promising to design organic solar cell development as well as for LED TVs.

REFERENCES

[1] S. A. Maier, *Plasmonics: Fundamentals and Applications*. New York, NY: Springer US, 2007.

[2] M. A. White, *Properties of materials*, New York, NY: Oxford University Press,1999.

[3] J. Shibayama, K. Shimizu, J. Yamauchi, and H. Nakano, "Surface Plasmon Resonance Waveguide Sensor in the Terahertz Regime", *Journal of Lightwave Technology*, vol. 34, no. 10, pp. 2518–2525, 2016.

[4] C. Han, Y. Chu, Z. Wang, and X. Zhao, , "Spoof surface plasmonic waveguide devices with compact length and low-loss", *Journal of Applied Physics*, vol. 122, no. 12, pp. 123-301, Jul 2017.

[5] Y. Fang, and M. Sun, "Nanoplasmonic waveguides: towards applications in integrated nanophotonic circuits", *Light: Science and Applications*, vol. 4, no.6, Jun 2015.

[6] Z. Zhang, and J. Wang, "Long-range hybrid wedge plasmonic waveguide", *Scientific Reports*, vol. 4, no.1, Nov 2014.

[7] C. S. Perera, A. M. Funston, H.-H. Cheng, and K. C. Vernon, "Mapping bound plasmon propagation on a nanoscale stripe waveguide using quantum dots: influence of spacer layer thickness", *Beilstein Journal of Nanotechnology*, vol.6, pp.2046–2051, Oct 2015.

[8] O. Krupin, and P. Berini, "Long-Range Surface Plasmon-Polariton Waveguide Biosensors for Human Cardiac Troponin I Detection", *Sensors*, vol.19, no. 3, pp. 631-637, Oct 2019.

[9] L. Wei, S. Aldawsari, and B. R. West, "Theoretical Analysis of Plasmonic Modes in a Symmetric Conductor–Gap–Dielectric Structure for Nanoscale Confinement", *IEEE Photonics Journal*, vol. 6, no. 3, pp. 1–10, Jun 2014.

[10] M. A. Islam, and M. S. Alam, "An Extremely Large Mode Area Microstructured Core Leakage Channel Fiber With Low Bending Loss", *Journal of Lightwave Technology*, vol. 32, no. 2, pp. 250–256, Jan 2014.

[11] P. Sharma, and V. D. Kumar, "Hybrid Insulator Metal Insulator Planar Plasmonic Waveguide-Based Components", *IEEE Photonics Technology Letters*, vol. 29, no. 16, pp. 1360–1363, Aug 2017.

[12] Y. Shi, K. Zheng, Y. Su, and Y. Wang, "Long-Range Slot Hybrid Surface Plasmon Waveguide With Long Propagation Distance and Tight Mode Confinement", *Fiber and Integrated Optics*, vol. 36, no. 3, pp. 104–110, May 2017.

[13] S. Chitimireddy, P. Sharma, and D. K. Vishwakarma, "Sinusoidal Bragg grating based on hybrid metal insulator metal plasmonic waveguide", *Micro and Nano Letters*, vol. 13, no. 11, pp. 1633–1637, Jul 2018.

[14] R. R. Khan, and M. Z. Islam, "Numerical investigation of a hybrid plasmonic waveguide for subwavelength confinement of light", *Proceedings of International Conference on Telecommunications and Photonics (ICTP)*, pp. 217–221, Dec 2017.

[15] S. Deng, A. K. Yetisen, K. Jiang, and H. Butt, "Computational modelling of a graphene Fresnel lens on different substrates", *RSC Adv.*, vol. 4, no. 57, pp. 30050–30058, May 2014.

[16] S. T. D. Irawan, "Graphene Dual Properties, Mobility and Polarisibility: The Challenge", *Journal of Biosensors and Bioelectronics*, vol. 05, no. 03, Jun 2014.

[17] I.-T. Lin, C. Fan, and J.-M. Liu, "Propagating and Localized Graphene Surface Plasmon Polaritons on a Grating Structure", *IEEE Journal of Selected Topics in Quantum Electronics*, vol. 23, no. 1, pp. 144–147, Feb 2017.

[18] W. Kong, Y. Wan, W. Zhao, S. Li, and Z. Zheng, "Bloch-Surface-Polariton-Based Hybrid Nanowire Structure for Subwavelength, Low-Loss Waveguiding", *Applied Sciences*, vol. 8, no. 3, pp. 358-365, Mar 2017.
[19] G. P. Agrawal, "*Fiber-optic communication systems",* Oxford: Wiley-Blackwell, 2011.
[20] K. Yao, R. Unni, and Y. Zheng, "Intelligent nanophotonics: merging photonics and artificial intelligence at the nanoscale", *Nanophotonics*, vol. 8, no. 3, pp. 339–366, Jan 2019.
[21] D. A. Kuzmin, I. V. Bychkov, V. G. Shavrov, and V. V. Temnov, "Plasmonics of magnetic and topological graphene-based nanostructures", *Nanophotonics*, vol. 7, no. 3, pp. 597–611, Mar 2018 .
[22] M.-T. Wei, J. Ng, C. T. Chan, A. Chiou, and H. D. Ou-Yang, "Transverse force profiles of individual dielectric particles in an optical trap", *Optical Trapping and Optical Micromanipulation IX*, pp. 8458–8465, Jan 2012.
[23] P. Malara, A. Crescitelli, V. D. Meo, A. Giorgini, S. Avino, and E. Esposito, "Resonant enhancement of plasmonic nanostructured fiber optic sensors", *Sensors and Actuators B: Chemical*, vol. 273, pp. 1587–1592, Jul 2018.
[24] S. Zarei, A. Mataji-Kojouri, M. Shahabadi, and S. Mohajerzadeh, "Tunable terahertz filter composed of an array of subwavelength metallic ring apertures", *Optik*, vol. 164, pp. 355–361, Mar 2018 .
[25] J. Etxebarria, J. Ortega, and C. L. Folcia, "Enhancement of the optical absorption in cholesteric liquid crystals due to photonic effects: an experimental study", *Liquid Crystals*, vol. 45, no. 1, pp. 122–128, Sep 2017.
[26] P. Bharadwaj, B. Deutsch, and L. Novotny, "Optical antennas.", *Advances in Optics and Photonics*, vol. 1, no. 3, pp. 438–483, Aug 2009.
[27] H. Nasari, M. S. Abrishamian, and P. Berini, "Nonlinear optics of surface plasmon polaritons in subwavelength graphene ribbon resonators", *Optics Express*, vol. 24, no. 1, pp. 708–718, Jul 2016 .
[28] S. H. Mazharimousavi, A. Roozbeh, and M. Halilsoy, "Electromagnetic wave propagation through inhomogeneous material layers", *Journal of Electromagnetic Waves and Applications*, vol. 27, no. 16, pp. 2065–2074, Sep 2013.
[29] X. Yang, Y. Liu, R. F. Oulton, X. Yin, and X. Zhang, "Optical Forces in Hybrid Plasmonic Waveguides ", *Nano Letters*, vol. 11, no. 2, pp. 321–328, Jan 2011.
[30] A. C. Atre, A. García-Etxarri, H. Alaeian, and J. A. Dionne, "Metamaterials: A Broadband Negative Index Metamaterial at Optical Frequencies" , *Advanced Optical Materials*, vol. 1, no. 4, pp. 350–350, Apr 2013.
[31] A. P. Slobozhanyuk, P. V. Kapitanova, D. S. Filonov, D. A. Powell, I. V. Shadrivov, M. Lapine, Y. S. Kivshar, "Nonlinear interaction of meta-atoms through optical coupling", *Applied Physics Letters*, vol. 104, no. 1, pp. 014104–014113, Jan 2014 .
[32] D. Schumacher, C. Rea, D. Heitmann, K. Scharnberg, "Surface plasmons and Sommerfeld–Zenneck waves on corrugated surfaces", *Surface Science*, vol. 408, no. 1–3, pp. 203-211, Feb 2019.
[33] Andrey A. Bogdanov, Kirill L. Koshelev, Polina V. Kapitanova, Mikhail V. Rybin, Sergey A. Gladyshev, Zarina F. Sadrieva, Kirill B. Samusev, Yuri S. Kivshar, and Mikhail F. Limonova , "Bound states in the continuum and Fano resonances in the strong mode coupling regime", Advance Photonics, vol. 1, no. 1, pp. 016001-1-126, May 2019.
[34] P. B. Johnson, R. W. Christy, , "Optical Constants of the Noble Metals", *Physical Review B*, vol. 6(12), pp. 4370-4379, Jan 1972.

[35] J. Mu, L. Chen, X. Li, W.-P. Huang, L. C. Kimerling, and J. Michel, "Hybrid nano ridge plasmonic polaritons waveguides", *Applied Physics Letters*, vol. 103, no. 13, pp. 131107-131114, Sep 2013.
[36] T. Wu, and Y.-W. Lin, "Surface-enhanced Raman scattering active gold nanoparticle/nanohole arrays fabricated through electron beam lithography", *Applied Surface Science*, vol. 435, no. 37, pp. 1143–1149, Nov 2017.
[37] Y. Bian, and Q. Gong, "Bow-Tie Hybrid Plasmonic Waveguides", *Journal of Lightwave Technology*, vol. 32, no. 23, pp. 4504–4509, Jun 2013 .
[38] Q. Cao, S.-J. Han, and G. S. Tulevski, "Fringing-field dielectrophoretic assembly of ultrahigh-density semiconducting nanotube arrays with a self-limited pitch", *Nature Communications*, vol. 5, no. 1, pp. 574-588, Sep 2014.
[39] G. R. Liu, and S. S. Quek, *The finite element method: a practical course*. Amsterdam: Butterworth-Heinemann.
[40] T. Nurmohammadi, K. Abbasian,and R. Yadipour, " Numerical study of dumbbell-shaped gold nanoparticles using in plasmonic waveguides in near infra-red spectrums" , *Optical and Quantum Electronics*, vol. 50, no. 4, pp. 435–442, Mar 2018.
[41] J. Polanco, R. M. Fitzgerald, and A. A. Maradudin, "Scattering of an Obliquely Incident Surface Plasmon Polariton from Sub-Micron Metal Grooves and Ridges", *Plasmonics*, vol. 10, no. 5, pp. 1173–1183, Mar 2015.
[42] X. He, T. Ning, S. Lu, J. Zheng, J. Li, R. Li, and L. Pei, "Ultralow loss graphene-based hybrid plasmonic waveguide with deep-subwavelength confinement". *Optics Express*, vol. 26, no. 8, pp. 10109-10118, Apr 2018.
[43] W. Zhou, and X. G. Huang, "Long-Range Air-Hole Assisted Subwavelength Waveguides: Towards Large-Scale Photonic Integration", *Advanced Materials Research*, vol. 901, no. 40, pp. 65–69, Feb 2014.
[44] L. Chen, T. Zhang, and X. Li, "Enhanced Optical Forces by Hybrid Long-Range Plasmonic Waveguides" , *Journal of Lightwave Technology*, vol. 31, no. 21, pp. 3432–3438, Jan 2013.
[45] COMSOL Multiphysics, version 4.4.
[46] M. S. Islam, and M. S. Alam, "Effect of Lower Index Dielectric Coating on Plasmon Polaritons Guided by Finite Metal Stripes". *Proceedings of 1st International Conference on Telecommunication and Photonics (ICTP).IAC, BUET, Dhaka,* pp. 1-4, Oct 2015.
[47] Jitender, A. Kumar, R. K. Varshney, and M. Kumar, "Calculation of propagation characteristics of surface plasmons in gold/silver nanowires" , *Applied Optics*, vol. 54, no. 12, pp. 3715-3720, Apr 2015.
[48] T. Sharma, and M. Kumar, "Hybridization of plasmonic and photonic modes for subwavelength optical confinement with longer propagation and variable nonlinearity", o*ptics Communications*, vol. 343, pp. 85–90, Jan 2015.
[49] K. F. Fiaboe, P. Kumar, and J. S. Roy, "Flattened zero dispersion Photonic crystal fibers with embedded nano holes and ultra low confinement loss for supercontinuum generation", *Advanced Electromagnetics*, vol. 8, no. 4, pp. 7–15, 2019
[50] G. X. Cai, M. Luo, Z. P. Cai, H. Y. Xu, and Q. H. Liu, "A Slot-Based Surface Plasmon-Polariton Waveguide With Long-Range Propagation and Super confinement", *IEEE Photonics Journal*, vol. 4, no. 3, pp. 844-855, June 2012.

PUBLICATIONS

[1] M. S. Alam, and M. S. Alam, "Propagation of Surface Plasmon Polaritons in Hybrid Waveguide with Metal Cap and Graphene Layer". *Proceedings of 4th International Conference on Electrical Engineering and Information & Communication Technology (ICEEICT, MIST, Dhaka,* pp. 506-509, Dec 2018.